



Grilli, N., Tarleton, E., & Cocks, A. C. F. (2021). Coupling a discrete twin model with cohesive elements to understand twin-induced fracture. *International Journal of Fracture*, 227(2), 173-192.
<https://doi.org/10.1007/s10704-020-00504-9>

Publisher's PDF, also known as Version of record

License (if available):
CC BY

Link to published version (if available):
[10.1007/s10704-020-00504-9](https://doi.org/10.1007/s10704-020-00504-9)

[Link to publication record in Explore Bristol Research](#)
PDF-document

This is the final published version of the article (version of record). It first appeared online via Springer at <https://doi.org/10.1007/s10704-020-00504-9> .Please refer to any applicable terms of use of the publisher.

University of Bristol - Explore Bristol Research

General rights

This document is made available in accordance with publisher policies. Please cite only the published version using the reference above. Full terms of use are available:
<http://www.bristol.ac.uk/red/research-policy/pure/user-guides/ebr-terms/>



Coupling a discrete twin model with cohesive elements to understand twin-induced fracture

Nicolò Grilli · Edmund Tarleton · Alan C. F. Cocks

Received: 20 August 2020 / Accepted: 26 November 2020 / Published online: 2 February 2021
© The Author(s) 2021

Abstract The interplay between twinning and fracture in metals under deformation is an open question. The plastic strain concentration created by twin bands can induce large stresses on the grain boundaries. We present simulations in which a continuum model describing discrete twins is coupled with a crystal plasticity finite element model and a cohesive zone model for intergranular fracture. The discrete twin model can predict twin nucleation, propagation, growth and the correct twin thickness. Therefore, the plastic strain concentration in the twin band can be modelled. The cohesive zone model is based on a bilinear traction-separation law in which the damage is caused by the normal stress on the grain boundary. An algorithm is developed to generate interface elements at the grain boundaries that satisfy the traction-separation law. The model is calibrated by comparing polycrystal simulations with the experimentally observed strain to failure and maximum stress. The dynamics of twin and crack nucleation have been investigated. First, twins nucleate and propagate in a grain, then, microcracks form near the intersection between twin tips and grain boundaries. Microcracks appear at multiple locations before

merging. A propagating crack can nucleate additional twins starting from the grain boundary, a few micrometres away from the original crack nucleation site. This model can be used to understand which type of texture is more resistant against crack nucleation and propagation in cast metals in which twinning is a deformation mechanism. The code is available online at <https://github.com/TarletonGroup/CrystalPlasticity>.

Keywords Crystal plasticity · Fracture · Cohesive zone modelling · Twinning · Uranium

1 Introduction

Intergranular fracture is a type of brittle fracture, which involves the nucleation and propagation of cracks along grain boundaries. It is a dominant failure mechanism in as-cast metals (Powell 1994), ultrafine-grained metals (Pippan and Hohenwarter 2016), during stress corrosion (Birbilis and Hinton 2011) and hydrogen embrittlement (Barrera et al. 2018; Elmukashfi et al. 2020). It takes place in materials in which the stress required to debond the grain boundary interface is lower than the stress to debond atomic planes inside the grains (Jiang et al. 2015) or to nucleate and grow microscopic voids (Tvergaard 1981; Cocks and Ashby 1982).

Plastic deformation, induced by the motion of dislocations and by twinning (Christian 2002), has an important effect on fracture. The interplay between plasticity and fracture is complex, because it depends on the load condition (Sistaninia and Niffeneger 2015; Grilli

N. Grilli (✉) · E. Tarleton · A. C. F. Cocks
Department of Engineering Science, University of Oxford,
Parks Road OX1 3PJ, UK
e-mail: nicolo.grilli@eng.ox.ac.uk

E. Tarleton
Department of Materials, University of Oxford,
Parks Road OX1 3PH, UK
e-mail: edmund.tarleton@eng.ox.ac.uk

and Koslowski 2018), on the microstructure (Qian et al. 2018) and on the presence of pre-existing cracks (Duarte et al. 2018). Larger plastic deformation leads to stress relaxation and can retard the propagation of pre-existing cracks (Grilli and Koslowski 2019). In this case, a larger strain to failure is observed (Woelke et al. 2015). However, plasticity can also cause damage initiation because its anisotropic nature leads to stress variations at the microscale (Krupp 2007).

Plastic deformation at the scale of the grain-size in metals is an inhomogeneous phenomenon. It is concentrated into slip bands or twins, depending on the stacking fault energy (Frøseth et al. 2005), and can favour crack nucleation (Tanaka and Mura 1981). However, shear bands emanating from the notch of a tensile sample can delay fracture (Li et al. 2016). A plastically deforming band that impinges on a grain boundary leads to a normal stress that decreases with the band thickness (Sauzay and Moussa 2013). High stress exists in the vicinity of a twin tip, which can induce slip ahead of it when the twin tip terminates inside the grain (Sleeswyk 1962).

There is experimental evidence of the correlation between twinning and fracture (Christian and Mahajan 1995). Most metals that exhibit brittle fracture at low temperature also deform by mechanical twinning (O'Neill 1926). Microcracks in TWIP steels form at intersecting twins and propagate both along grain boundaries and along twin interfaces (Koyama et al. 2013). Microcracks have also been observed near the intersection between impinging twin bands and grain boundaries in the intermetallic TiAl (Bieler et al. 2005). The weaker boundaries have been identified as the ones in which the neighbouring grains cannot accommodate the twin strain. Cracks have been observed near the intersection between twins and grain boundaries in several BCC metals at low temperatures (Cr, W, Mo) (Marcinkowski and Lipsitt 1962; Gilbert et al. 1964). The grain size dependence of the stress to nucleate twins and cracks are similar. However, it is not clear if a twin induces crack nucleation or vice-versa. The same properties are observed in α -uranium, which is the material of interest in the present paper (Taplin 1964; Taplin and Martin 1965). α -uranium exhibits intergranular fracture in the temperature range from -100 °C to 200 °C (Collins and Taplin 1978), while ductile fracture (Taplin and Cocks 1967) and inclusion cracking are observed at higher temperatures (Davies and Martin 1961).

Imaging techniques such as differential aperture X-ray microscopy (Balogh et al. 2013) and high-resolution electron backscatter diffraction (EBSD) (Abdolvand and Wilkinson 2016) have been used to measure the elastic strain field near the twin tip and at the twin interface (Hubbell and Seltzer 1995). However, the large X-ray absorption coefficient of α -uranium limits the applicability of the first technique (Hubbell and Seltzer 1995), the preparation of strain-free α -uranium surfaces for EBSD is challenging (Sutcliffe et al. 2019; Earp et al. 2018) and X-ray transmission integrates the signal over the thickness of the sample (Irastorza-Landa et al. 2016, 2017b), limiting the ability to image individual twins. In-situ techniques, which can reveal the chronological order of twin and crack nucleation and propagation, are needed but the characteristic time during which microcracks and twins nucleate is very short, as they propagate close to the speed of sound in the material (Oberson and Ankem 2005). A unique example in the literature is the measurement of the magnetic properties with microsecond time resolution, showing that twinning takes place a few microseconds earlier than crack nucleation in iron-silicon (Williams and Reid 1971).

Several open questions remain. What is the effect of strain localization due to twinning on fracture? Which combinations of grain orientations favour intergranular fracture? How does the crack propagate once nucleated? What is the chronological order of events: do propagating cracks nucleate twins or vice-versa? What is the role of dislocations? These questions are particularly important because twinning can be inhibited using prestrain at a higher temperature (Boucher and Christian 1972) or by introducing precipitates (Chun et al. 1969).

Crystal plasticity finite element (CPFE) and fracture mechanics simulations are suitable to investigate these issues. CPFE is a computational finite strain method that takes into account the plastic deformation of slip and twin systems (Roters et al. 2018; Grilli 2016), and the reorientation of the crystal lattice due to twinning (Grilli et al. 2020d). The different orientations of neighbouring grains can be included and elastic strain incompatibility can be calculated, as well as the intergranular stress (Petkov et al. 2019).

Intergranular fracture can be described using a cohesive-zone model (Simonovski and Cizelj 2011). Elements of negligible thickness are used to describe the separation of the grain boundary interface. Traction-

separation relationships for interfaces were first introduced by Barenblatt (Barenblatt 1962). Softening of the interface element takes place after a critical value of the stress is reached; this allows both crack nucleation and propagation to be simulated. Camacho and Ortiz showed that cohesive-zone modelling is compatible with finite element modelling of the bulk material and is able to reproduce arbitrary crack paths between 2D bulk elements in a mesh (Camacho and Ortiz 1996). Ortiz and Pandolfi extended the method to 3D dynamic simulations (Ortiz and Pandolfi 1999).

The recent development of continuum models to describe discrete twins (Liu et al. 2018) allows us to simulate the concentration of plastic deformation in a narrow band. Twin nucleation and growth has been reproduced (Qiao et al. 2016). The coupling with phase field fracture has allowed twin nucleation induced by crack propagation from a notch to be studied (Clayton and Knap 2016; Grilli et al. 2018a). However, no models for twin-induced fracture are available.

It is fundamental that such a model can correctly predict the twin thickness and the stress for twin nucleation and growth. This is because the stress at the twin tip depends on the twin thickness (Sauzay and Moussa 2013). This has been achieved using a non-local model for the critical resolved shear stress (CRSS) for twinning, which has been validated using in-situ EBSD experiments (Grilli et al. 2020d).

In this paper, a coupled plasticity-fracture model is developed and applied to 3D polycrystal simulations. The model is calibrated using data in the literature from experiments on α -uranium. The effect of discrete twins on crack nucleation and propagation is investigated. Specific combinations of the orientations of neighbouring grains that favour or prevent intergranular fracture are investigated.

Section 2 describes the cohesive-zone model and the formulation of 3D interface elements. Section 3 describes the crystal plasticity model used for the mechanical behaviour of the grains and the coupling with a continuum model for twinning. In Sect. 4, polycrystal simulations are carried out to calibrate the parameters of the cohesive zone model. The details of crack nucleation and propagation at the grain boundaries are investigated in Sect. 5. In Sect. 6, the crack nucleation and propagation is studied in the case of non-columnar grains. Sections 7 and 8 contain discussion and conclusions.

2 Cohesive zone model and interface elements

Zero thickness interface elements are assigned to grain boundaries. An algorithm has been developed to automatically generate such interface elements in an arbitrary polycrystal (Grilli 2020). First, the mesh is generated with 3D hexahedral elements and zero thickness grain boundaries. Hexahedral elements are preferred to linear tetrahedral elements in crystal plasticity finite element simulations because they do not exhibit volumetric locking and a consequent stiff response during bending (Cheng et al. 2016). Then, nodes at the grain boundaries, which are shared by two or three grains, are duplicated or triplicated respectively. An example is shown in Fig. 1a. The original nodes 1, 2, 3, 4 belong to a grain boundary between grain 1 and grain 2. During the duplication, nodes 5, 6, 7, 8 are created, which have the same undeformed coordinates as nodes 1, 2, 3, 4 respectively. Grain 1 retains the original nodes 1, 2, 3, 4 while nodes 5, 6, 7, 8 are assigned to grain 2. Therefore, nodes 1, 2, 3, 4 belong to one hexahedral element in grain 1, while nodes 5, 6, 7, 8 belong to an element in grain 2.

An interface element is created that includes all the nodes from 1 to 8. This interface element connects the two hexahedral elements in grain 1 and 2. A bilinear traction-separation law, as shown in Fig. 1b, is used for the interface element to represent the cohesion forces of the grain boundaries (Barenblatt 1962). Because of the arbitrary orientation of each interface element in space, it is necessary to define a local reference system in which the separation vector $\mathbf{\Delta}$ is defined. This will be called the mid-plane reference system and it is defined as follows. $\hat{\mathbf{x}}_m$ is the unit vector that connects the mid-point m1 between node 1 and node 5 with the mid-point m2 between node 2 and node 6. The unit vector normal to the mid-plane $\hat{\mathbf{z}}_m$ is found by taking the cross product of $\hat{\mathbf{x}}_m$ and the direction that connects the mid-points m1 and m4. The third unit vector $\hat{\mathbf{y}}_m$ is calculated as:

$$\hat{\mathbf{y}}_m = \hat{\mathbf{z}}_m \times \hat{\mathbf{x}}_m . \quad (1)$$

The three orthogonal unit vectors ($\hat{\mathbf{x}}_m, \hat{\mathbf{y}}_m, \hat{\mathbf{z}}_m$) constitute the mid-plane reference system; its origin is in the middle of the quadrilateral with vertices m1, m2, m3, m4. This choice allows the traction-separation law in this coordinate system to be defined, which is independent of the orientation of the interface element. In the following, the separation vector $\mathbf{\Delta} = (\Delta_{s1}, \Delta_{s2}, \Delta_n)$

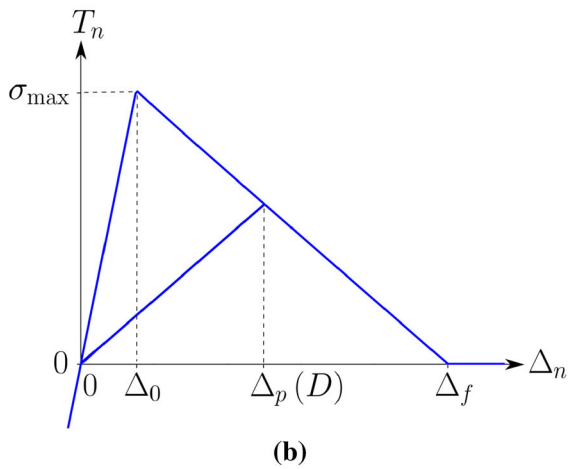
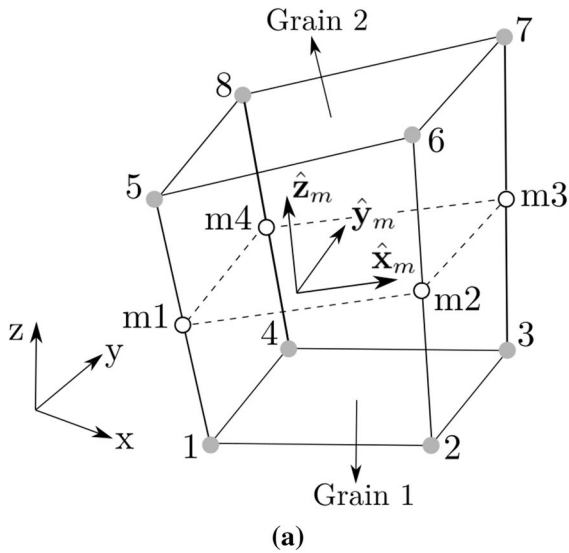


Fig. 1 **a** 3D cohesive elements with 8 nodes and **b** bilinear traction-separation law

is defined in the mid-plane reference system and can be calculated on the (\hat{x}_m, \hat{y}_m) plane using shape functions, as reported in Appendix A.

The cohesive force vector $\mathbf{T} = (T_{s1}, T_{s2}, T_n)$ is also expressed in the mid-plane reference frame. The traction/separation law is given by:

$$T_n = \begin{cases} K_n \Delta_n, & \text{if } D = 0 \text{ or } \Delta_n < 0, \\ 0, & \text{if } D = 1 \text{ and } \Delta_n > 0, \\ K_n (1 - D) \Delta_n, & \text{if } 0 < D < 1 \text{ and } 0 < \Delta_n < \Delta_p(D), \\ K_n \Delta_0 \frac{(\Delta_f - \Delta_n)}{(\Delta_f - \Delta_0)}, & \text{if } 0 < D < 1 \text{ and } \Delta_n > \Delta_p(D), \end{cases} \quad (2)$$

where $0 < D < 1$ is the damage variable, describing the degradation of the normal stiffness K_n . Δ_0 is the normal separation at which damage starts and Δ_f is the normal separation at which damage is complete, as shown in Fig. 1b. Given a damage D , $\Delta_p(D)$ is the normal separation at which the maximum normal traction is reached. If $\Delta_n > \Delta_p(D)$, damage increases and normal traction decreases. This formulation includes contact ($\Delta_n < 0$) during which damage does not affect the normal cohesive force.

In the present model, shear separation does not induce damage, but shear cohesive force is degraded by existing damage:

$$T_s = \begin{cases} G_s \Delta_s, & \text{if } D = 0, \\ 0, & \text{if } D = 1, \\ G_s (1 - D) \Delta_s, & \text{if } 0 < D < 1. \end{cases} \quad (3)$$

where $\Delta_s = \sqrt{\Delta_{s1}^2 + \Delta_{s2}^2}$ is the magnitude of the shear separation. If $D = 1$, there is no shear traction, even in the case of contact ($\Delta_n < 0$), i.e. the contact is assumed to be frictionless. The components of the shear traction along the axes \hat{x}_m and \hat{y}_m are:

$$T_{s1} = T_s \frac{\Delta_{s1}}{\Delta_s}, \quad (4)$$

$$T_{s2} = T_s \frac{\Delta_{s2}}{\Delta_s}. \quad (5)$$

The damage nucleation induced by shear separation is relevant in brittle materials (Chen and Ravichandran 1996, 1997) but has been neglected in the description of intergranular fracture in metals (Yamakov et al. 2006; Simonovski and Cizelj 2011).

It is of the utmost importance that the nodes of the cohesive elements are arranged as in Fig. 1a. If the positions of nodes 2 and 4 are exchanged, and the same for nodes 6 and 8, the unit vector \hat{z}_m would point in the opposite direction. In that case, according to the definition of the separation vector in Appendix A, interface opening ($\Delta_n > 0$) and contact ($\Delta_n < 0$) would be inverted and not reproduced correctly. The algorithm that generates the interface elements takes this issue into account (Grilli 2021).

The principle of virtual work provides the weak form of the equilibrium equations (Park and Paulino 2012):

$$\int_{\Omega} \delta \boldsymbol{\varepsilon} : \boldsymbol{\sigma} \, dV + \int_{\Gamma_c} \delta \boldsymbol{\Delta} \cdot \mathbf{T} \, dS = \int_{\Gamma} \delta \mathbf{u}_G \cdot \mathbf{T}_{\text{ext}} \, dS \quad (6)$$

where Ω is the representative volume, Γ_c is the cohesive interface and Γ is the boundary. The δ symbol represents the variation of a variable. $\boldsymbol{\varepsilon}$ is the strain tensor and $\boldsymbol{\sigma}$ is the Cauchy stress. \mathbf{u}_G is the displacement vector, expressed in the global reference frame, and \mathbf{T}_{ext} is the external force.

The second term on the left-hand side of Eq. (6) is introduced in the commercial finite element code Abaqus by using the UEL subroutine (Smith 2009). This requires us to define the contribution to the internal force vector $\mathbf{f}_{\text{coh}}^e$ for each cohesive element. Therefore, the variation $\delta\mathbf{A}$ has to be expressed as a function of the variation of the displacement vector $\delta\mathbf{u}_G$. This is done by using the \mathbf{B} matrix defined in Eq. (9.11) of Appendix A:

$$\delta\mathbf{A} = \mathbf{B} \delta\mathbf{U}, \quad (7)$$

where $\delta\mathbf{U} = (\delta\mathbf{u}_1, \delta\mathbf{u}_2, \delta\mathbf{u}_3, \delta\mathbf{u}_4, \delta\mathbf{u}_5, \delta\mathbf{u}_6, \delta\mathbf{u}_7, \delta\mathbf{u}_8)^T$ is a $[24 \times 1]$ vector that contains the variation of the displacement components of the eight nodes of the cohesive element. Since $\delta\mathbf{U}$ is expressed in the mid-plane reference frame, a transformation matrix \mathbf{M} is needed. \mathbf{M} is a $[24 \times 24]$ block diagonal matrix. It has eight equal $[3 \times 3]$ main-diagonal blocks. These blocks contain the $[3 \times 3]$ rotation matrix that transforms vectors from the global reference frame to the mid-plane reference frame. Therefore:

$$\delta\mathbf{A} = \mathbf{B}\mathbf{M} \delta\mathbf{U}_G, \quad (8)$$

where $\delta\mathbf{U}_G$ is the vector $\delta\mathbf{U}$ expressed in the global reference frame. Therefore, the contribution of a single cohesive element Γ_e to the second term on the left-hand side of Eq. (6) is given by:

$$\int_{\Gamma_e} \delta\mathbf{A}^T \mathbf{T} \, dS = \delta\mathbf{U}_G^T \left(\int_{\Gamma_e} \mathbf{M}^T \mathbf{B}^T \mathbf{T} \, dS \right) = \delta\mathbf{U}_G^T \mathbf{f}_{\text{coh}}^e, \quad (9)$$

where $\mathbf{f}_{\text{coh}}^e$ is the internal $[24 \times 1]$ force vector of the cohesive interface. The vector $\delta\mathbf{U}_G$ can be taken outside of the integral because it depends only on the displacements at the nodes. $\mathbf{f}_{\text{coh}}^e$ is calculated at 4 Gauss points, as described in Appendix A.

The Jacobian $\partial \mathbf{f}_{\text{coh}}^e / \partial \mathbf{U}_G$ which is calculated in the UEL subroutine is reported in Appendix B.

Table 1 Model parameters for the cohesive zone model

K_n	G_s	Δ_f
226.8 GPa/ μm	88.1 GPa/ μm	1 μm

The cohesive zone model parameters used in the following are reported in Table 1. The value of σ_{max} is calibrated in Sect. 4.

3 Crystal plasticity model

The behaviour of the grains is described using a crystal plasticity model coupled with a continuum model for discrete twins (Grilli et al. 2020b). A variable φ is used to represent discrete twins. It can increase from 0 (untwinned region) to 1 (fully twinned region). The model is introduced in Abaqus by using a UMAT subroutine (Smith 2009). An implicit CPFEM framework is used to calculate the increment of the Cauchy stress $\boldsymbol{\sigma}$ at each time step (Dunne et al. 2007). The rate of change of the corotational stress tensor is calculated using Hooke's law (Dunne and Petrinic 2006; Sakano et al. 2020):

$$\overset{\nabla}{\boldsymbol{\sigma}} = \mathbb{C} \dot{\boldsymbol{\varepsilon}}_c = \mathbb{C} (\dot{\boldsymbol{\varepsilon}} - \dot{\boldsymbol{\varepsilon}}_p), \quad (10)$$

where \mathbb{C} is the fourth order elasticity tensor (Fisher and McSkimin 1958). $\boldsymbol{\varepsilon}_e$, $\boldsymbol{\varepsilon}_p$ and $\boldsymbol{\varepsilon}$ are the elastic, plastic and total strain. \mathbb{C} is interpolated between the untwinned crystal lattice and the twinned crystal lattice when φ grows from 0 to 1.

Plastic deformation is described using the 8 most active slip systems of α -uranium at room temperature (McCabe et al. 2010). The twin system $[3\bar{1}0]$ (130) is used in the following simulations (Zhou et al. 2016).

The plastic strain rate is calculated by summing the contributions of the slip rates $\dot{\gamma}_\alpha(\boldsymbol{\sigma})$ on the slip systems and the contribution of the twinning rate (Kalidindi 1998):

$$\dot{\boldsymbol{\varepsilon}}_p = \frac{1}{2} \sum_{\alpha=1}^{N_{\text{slip}}} \dot{\gamma}_\alpha(\boldsymbol{\sigma}) (\mathbf{s}_\alpha \otimes \mathbf{n}_\alpha + \mathbf{n}_\alpha \otimes \mathbf{s}_\alpha) + \frac{1}{2} \dot{\varphi}(\boldsymbol{\sigma}, \varphi) \gamma_\beta^{\text{twin}} (\mathbf{s}_\beta \otimes \mathbf{n}_\beta + \mathbf{n}_\beta \otimes \mathbf{s}_\beta), \quad (11)$$

where s_α and n_α are the slip direction and normal of the slip system α . s_β and n_β are the twin direction and normal, and $\gamma_\beta^{\text{twin}}$ is the total shear produced by twinning. Given the total strain rate $\dot{\epsilon}$ in one time step, Eqs. (10)–(11) represent a non-linear system of equations in which the unknown is the Cauchy stress increment. They are solved using a Newton-Raphson algorithm (Dunne and Petrinic 2006).

The slip rates $\dot{\gamma}_\alpha(\sigma)$ are calculated using a power-law relationship (Grilli et al. 2015; Irastorza-Landa et al. 2017a):

$$\dot{\gamma}_\alpha(\sigma) = \dot{\gamma}_0 \left| \frac{\tau_\alpha}{\tau_\alpha^c} \right|^n \text{sign}(\tau_\alpha), \quad (12)$$

where $\dot{\gamma}_0$ and n are constants. τ_α is the resolved shear stress (RSS) on slip system α and τ_α^c is the CRSS (Roters 2011; Jafari et al. 2017). This rate-dependent law allows us to find a unique decomposition of the plastic strain increment into slip increments (Zamiri and Pourboghrat 2010). τ_α^c determines the hardening of the slip system and it is evolved in time using a dislocation density-based model, whose details are reported in (Beyerlein and Tomé 2008; McCabe et al. 2010; Grilli and Cocks 2019; Grilli et al. 2020a). The evolution of the dislocation densities is based on multiplication-annihilation rate equations (Kocks and Mecking 2003; Grilli et al. 2018b). This hardening model has been able to reproduce the elastic lattice strain in polycrystals measured using neutron diffraction (Grilli et al. 2020a) and the strain field inside individual grains measured using digital image correlation (Grilli et al. 2020c).

The time evolution of φ determines the nucleation and growth of discrete twins. It has two contributions:

$$\dot{\varphi}(\sigma, \varphi) = \dot{\varphi}_S(\sigma, \varphi) + \dot{\varphi}_G(\varphi), \quad (13)$$

the first term is a power-law relationship similar to the one used for slip (McCabe et al. 2010):

$$\dot{\gamma}_\beta^{\text{twin}} \dot{\varphi}_S(\sigma, \varphi) = \begin{cases} \dot{\gamma}_0 \left| \frac{\tau_\beta}{\tau_\beta^c(\varphi)} \right|^n, & \text{if } \tau_\beta > 0, \\ 0, & \text{if } \tau_\beta < 0. \end{cases} \quad (14)$$

This represents stress-induced twin nucleation, which takes place only when the RSS on the twin system is positive. The second term in Eq. (13) describes the driving force moving the atoms towards their equilibrium

position in the twinned crystal lattice, after they have passed the energy barrier for twinning (Liu et al. 2019):

$$\dot{\varphi}_G(\varphi) = \begin{cases} f(1 - \varphi), & \text{if } \varphi > \frac{1}{2}, \\ 0, & \text{if } \varphi < \frac{1}{2}. \end{cases} \quad (15)$$

$\varphi = 0.5$ corresponds to the maximum of the energy barrier and $1/f$ is a characteristic time interval during which the twin process completes.

The CRSS for twinning $\tau_\beta^c(\varphi)$ has two contributions:

$$\tau_\beta^c(\varphi) = \tau_0(\varphi) + \tau_{\text{twin}}(\varphi). \quad (16)$$

The first term $\tau_0(\varphi)$ models the twin nucleation and stress relaxation during twin propagation, as observed experimentally (Lynch et al. 2014), using a bilinear law:

$$\tau_0(\varphi) = \begin{cases} \frac{\tau_0}{4} + \frac{3\tau_0}{4}(1 - 2\varphi), & \text{if } \varphi < \frac{1}{2}, \\ \frac{\tau_0}{4} + \frac{3\tau_0}{4}(2\varphi - 1), & \text{if } \varphi > \frac{1}{2}, \end{cases} \quad (17)$$

where τ_0 is a constant.

$\tau_{\text{twin}}(\varphi)$ models the interaction between the twin interface and mobile dislocations (Ojha et al. 2014). When a mobile dislocation intersects a pre-existing twin boundary, it is decomposed into a sessile residual dislocation and a twinning dislocation. New twin layers are formed by the motion of these twinning dislocations, i.e. twin growth. The accumulation of residual dislocations prevents further mobile dislocations from interacting with the twin interface, leading to a higher CRSS for twin growth. The specific interaction depends on the dislocations character and on the direction from which they approach the twin interface (Gong et al. 2018). In this paper, we model this process with a non-local term that quantifies the total thickness of the twinned region in the neighbourhood of a point, which is also proportional to the density of residual dislocations:

$$\tau_{\text{twin}}(\varphi) = \frac{\tau_{\text{twin}}^0}{\Omega_c} \int_{\Omega_c} \varphi \, dV, \quad (18)$$

where τ_{twin}^0 is a constant. In order to quantify the thickness of the twinned region, the integration region Ω_c is chosen as a cylinder with height l_0 and radius r_0 ,

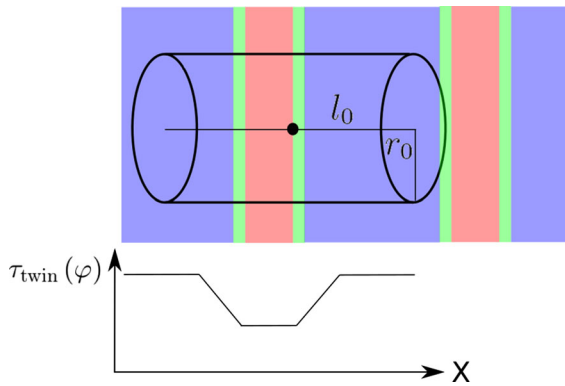


Fig. 2 Cylindrical integration volume used to calculate the term $\tau_{\text{twin}}(\varphi)$ of the CRSS for twinning

centred on the point considered, as shown in Fig. 2. Only integration points where the twin has overcome the energy barrier ($\varphi > 1/2$) are considered when evaluating the integral.

As shown in Fig. 2, given an axis X perpendicular to the twin planes, the term $\tau_{\text{twin}}(\varphi)$ can be evaluated. If the point considered moves towards the right and the cylindrical volume intersects the second twin on the right, the term $\tau_{\text{twin}}(\varphi)$ increases. This prevents the further growth of the twin on the left. The smooth increase of the term $\tau_{\text{twin}}(\varphi)$ in the presence of the pre-existing twins leads to the formation of smooth twin interfaces, in which φ varies from 1 to 0 along a certain length scale. This prevents the formation of sharp interfaces between twinned and untwinned regions that could not be captured properly by a finite element model.

It has been shown that this formulation can reproduce the nucleation and growth of discrete twins at the correct value of stress and with thickness as observed in EBSD experiments (Grilli et al. 2020d).

α -uranium (orthorhombic) material parameters are used for the plasticity model in the following simulations (Grilli et al. 2020a). They are reported in Table 2. The crystal plasticity code is available in the following repository: <https://github.com/TarletonGroup/CrystalPlasticity> (Tarleton 2020).

4 Polycrystal simulation and model calibration

In this section polycrystal simulations are carried out; the maximum stress and strain to failure are compared with experiments in the literature. A calibration of the cohesive zone model parameters is pro-

Table 2 Model parameters for the crystal plasticity model

τ_0	τ_{twin}^0	l_0	r_0	f	$\dot{\gamma}_0$	n	$\gamma_{\beta}^{\text{twin}}$
25 MPa	2000 MPa	10 μm	1 μm	1	s^{-1}	0.001 s^{-1}	20 0.299

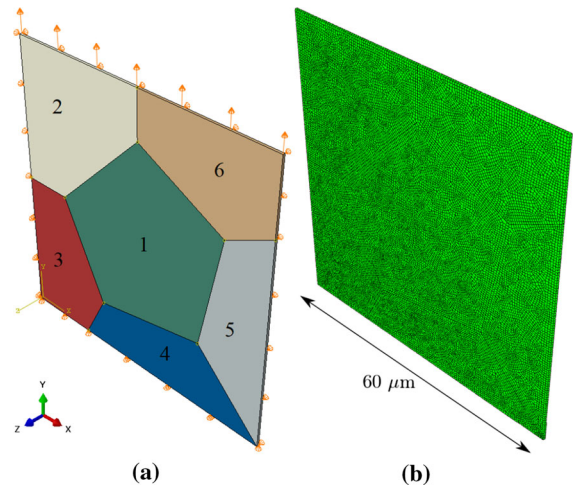


Fig. 3 Polycrystal simulation representative volume: **a** boundary conditions, different colours represent different grains; **b** mesh

posed. The columnar grain structure is shown in Fig. 3a and grains are numbered from 1 to 6. The representative volume is a parallelepiped with size $60 \mu\text{m} \times 60 \mu\text{m} \times 0.5 \mu\text{m}$. The mesh, shown in Fig. 3b, is constituted of hexahedral elements with average size $0.5 \mu\text{m}$. Cohesive elements are placed along the grain boundaries, including triple junctions.

Boundary conditions, modelling pure tension, are shown in Fig. 3a. $u_z = 0$ is imposed on the surface $z = 0$, $u_y = 0$ is imposed on the surface $y = 0$, $u_x = 0$ is imposed on the surface $x = 0$. A displacement u_y is imposed on the surface $y = 60 \mu\text{m}$. This displacement increases linearly with time, from 0 to $18 \mu\text{m}$, inducing an average strain up to 30%. The applied macroscopic strain rate used in all the following simulations is 0.001s^{-1} .

The orientation of the crystal lattice of the i -th grain in Fig. 3a is determined by rotation matrices \mathbf{R}_i . These rotation matrices transform a vector from the crystal lattice reference frame into the global reference frame, shown in Fig. 3a. The rotation matrix for grain number 1 is:

Table 3 Misorientation angles of the different grains in Fig. 3a

θ_2	θ_3	θ_4	θ_5	θ_6
$+\theta$	$-\theta$	-2θ	$+2\theta$	$-\theta$

$$\mathbf{R}_1 = \begin{pmatrix} -0.1834 & 0.983 & 0 \\ 0.983 & 0.1834 & 0 \\ 0 & 0 & -1 \end{pmatrix}. \quad (19)$$

This matrix aligns the direction of the twin system $[3\bar{1}0]$ (130) at 45° in the (x,y) plane and so the Schmid factor of this twin system in grain number 1 becomes 0.5. The rotation matrix for the i -th grain is found by multiplying \mathbf{R}_1 by a rotation around the z axis:

$$\mathbf{R}_i = \begin{pmatrix} \cos \theta_i & -\sin \theta_i & 0 \\ \sin \theta_i & \cos \theta_i & 0 \\ 0 & 0 & 1 \end{pmatrix} \cdot \mathbf{R}_1. \quad (20)$$

The angle θ_i for each grain is reported in Table 3. The angle θ quantifies the magnitude of the misorientation between the six grains.

The value of the separation to failure Δ_f is fixed at 1 μm . Simulations are carried out with different values of σ_{\max} , the damage initiation stress shown in Fig. 1b. The stress–strain curves, obtained by averaging the stress component σ_{yy} on the load surface $y = 60 \mu\text{m}$ in Fig. 3a, are shown in Fig. 4.

The maximum stress and strain to failure are strongly dependent on σ_{\max} , as shown in Fig. 4a. Tensile stresses up to 310 MPa have been measured in tensile bar experiments on coarse-grained α -uranium without reaching failure (Grilli et al. 2020a, c, d). This represents a lower limit for the calibration. As shown in Fig. 4a, this lower bound is satisfied if $\sigma_{\max} \geq 500$ MPa. Additionally, Huddart and Harding measured a strain to failure around $\varepsilon_f = 20\%$ for cast α -uranium at low strain rate (Huddart et al. 1980). This condition is approximately satisfied in the present simulations if $\sigma_{\max} = 650$ MPa. Values of σ_{\max} larger than 700 MPa leads to an unrealistically high strain to failure. Therefore, the value $\sigma_{\max} = 650$ MPa will be used in all the following simulations, which leads to a fracture energy of $\frac{1}{2}\sigma_{\max}\Delta_f = 325 \text{ J/m}^2$ and opening of $\Delta_0 = 2.87 \text{ nm}$ at damage initiation.

Figure 4b shows the stress–strain curves for different values of the misorientation angle θ . The lowest misorientation $\theta = 5^\circ$ shows the maximum stress and

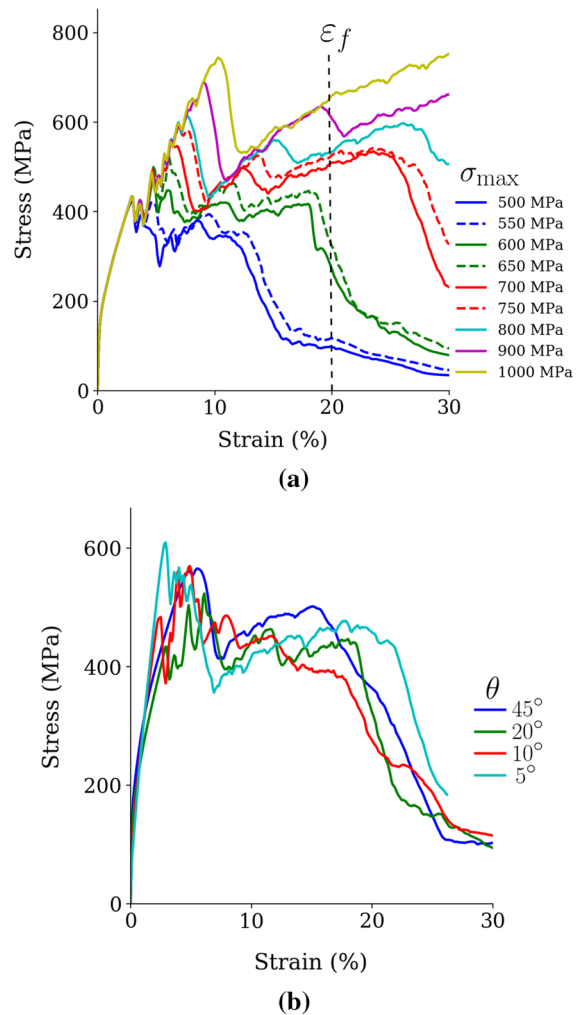


Fig. 4 a Stress–strain curves for different values of σ_{\max} used for model calibration. b Stress–strain curves for different misorientation angle θ

the maximum strain to failure. However, the relationship between strain to failure and misorientation angle θ does not monotonically decrease. The strain to failure for $\theta = 45^\circ$ is slightly larger than for $\theta = 20^\circ$. The dependence on the misorientation angle confirms that the previous calibration of σ_{\max} is not strongly dependent on the choice of the texture and, therefore, it is reliable.

Fig. 5 shows the twin variable φ and fracture path at 23% average strain for three different misorientation angles θ . The discrete twins ($\varphi = 1$) and their misorientations between neighbouring grains can be observed. The fracture path is similar for the three misorienta-

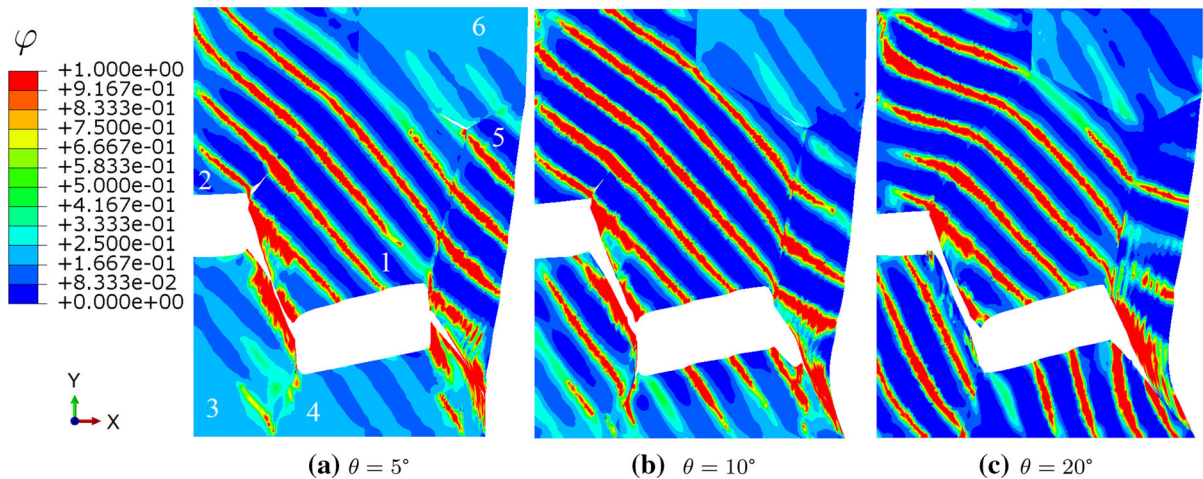


Fig. 5 Twin variable φ and fracture in the polycrystal at 23% strain for different grain misorientations θ

tions. The boundaries between grains 1-4 and between grains 2-3 are the first to completely damage. These are the boundaries with an orientation almost perpendicular to the load direction. They also have several discrete twins impinging on them from grains 1, 3, 4. The only difference in the fracture path is visible in Fig. 5a: a crack initiates at the grain boundary between grains 1-6 at the triple junction between grains 1, 5, 6. A discrete twin impinges on the triple junction from grain 5.

5 Crack initiation and propagation

In order to investigate the effect of twin tips impinging on a grain boundary, a three grains simulation is carried out, as shown in Fig. 6. The two grain boundaries have the same orientation with respect to the load direction; therefore, the effect of the twin orientation can be decoupled from the effect of the grain boundary orientation with respect to the load direction.

The representative volume is a parallelepiped with size $50 \mu\text{m} \times 80 \mu\text{m} \times 0.5 \mu\text{m}$. The mesh, shown in Fig. 6b, is constituted of hexahedral elements with average size $0.5 \mu\text{m}$. Three crystals are present, as shown in Fig. 6a, and cohesive elements are placed at the two grain boundaries.

Boundary conditions are shown in Fig. 6a. $u_y = 0$ is imposed on the surface $y = 0$ and a displacement u_y is imposed on the surface $y = 80 \mu\text{m}$. This displacement increases linearly with time. $u_x = 0$ is imposed

at the point $(25, 0, 0) \mu\text{m}$ and $u_z = 0$ is imposed at the points $(25, 0, 0) \mu\text{m}$, $(0, 0, 0) \mu\text{m}$, $(50, 0, 0) \mu\text{m}$. These boundary conditions allow the grains to rotate during tensile loading. The effect of this rotation can be studied in these simulations.

The orientation of the crystal lattice of the grains in Fig. 6a is determined by the following rotation matrices for texture 1 (T1):

$$\begin{aligned} \text{T1 : } R_1 &= \begin{pmatrix} -0.1834 & 0.983 & 0 \\ 0.983 & 0.1834 & 0 \\ 0 & 0 & -1 \end{pmatrix}, \\ R_2 &= \begin{pmatrix} -0.3513 & 0.9362 & 0 \\ 0.9362 & 0.3513 & 0 \\ 0 & 0 & -1 \end{pmatrix}, \\ R_3 &= \begin{pmatrix} -0.983 & -0.1834 & 0 \\ -0.1834 & 0.983 & 0 \\ 0 & 0 & -1 \end{pmatrix}, \end{aligned} \quad (21)$$

and texture 2 (T2):

$$\begin{aligned} \text{T2 : } R_1 &= \begin{pmatrix} -0.1834 & 0.983 & 0 \\ 0.983 & 0.1834 & 0 \\ 0 & 0 & -1 \end{pmatrix}, \\ R_2 &= \begin{pmatrix} -0.983 & -0.1834 & 0 \\ -0.1834 & 0.983 & 0 \\ 0 & 0 & -1 \end{pmatrix}, \\ R_3 &= \begin{pmatrix} -0.3513 & 0.9362 & 0 \\ 0.9362 & 0.3513 & 0 \\ 0 & 0 & -1 \end{pmatrix}. \end{aligned} \quad (22)$$

Fig. 6 Polycrystal simulation to study crack propagation: **a** grains and boundary conditions, **b** mesh and node path used to analyse damage evolution

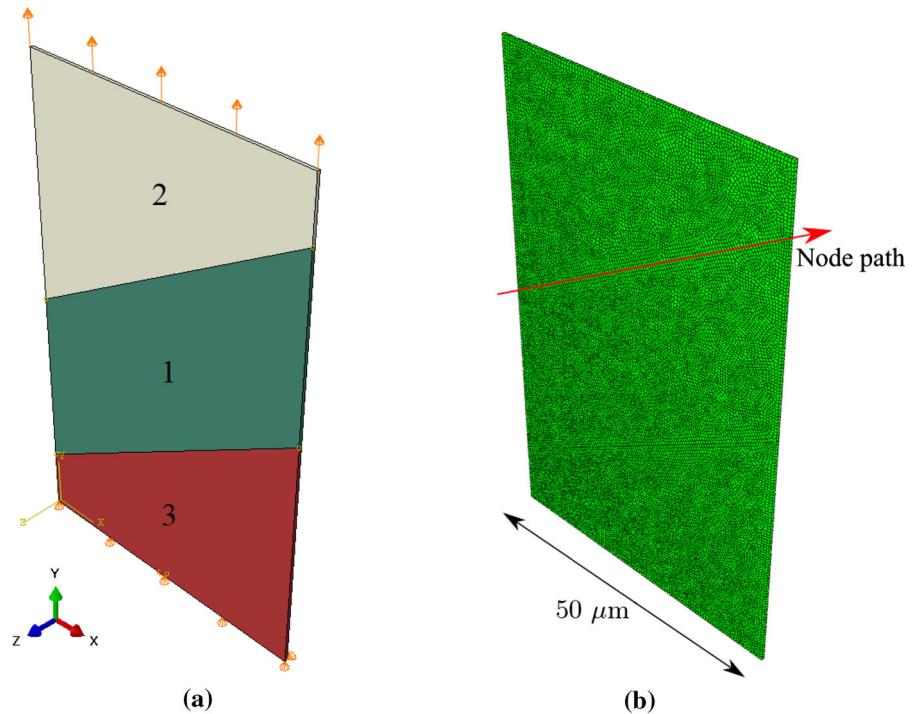
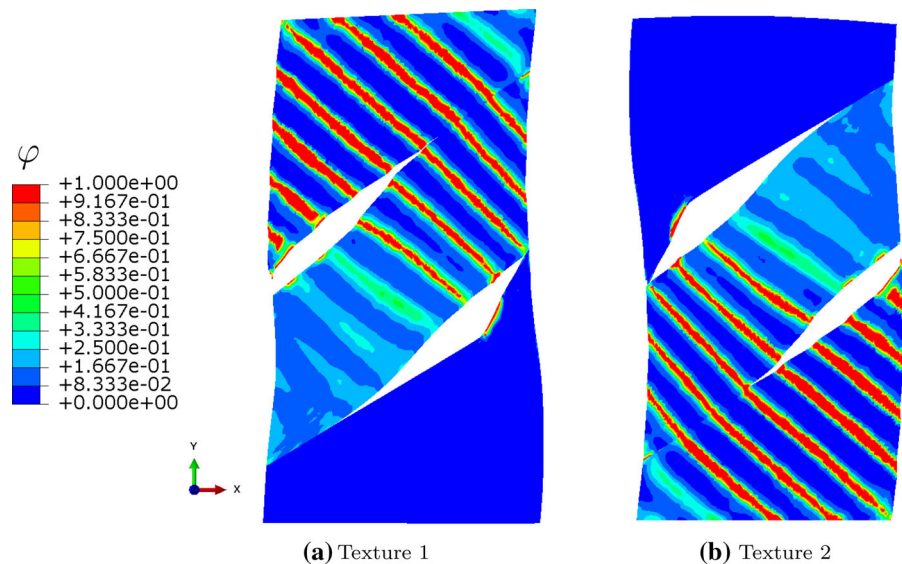


Fig. 7 Twin variable φ and fracture at 12.5% strain



The twin variable φ and fracture path are shown in Fig. 7 for the two different textures at 12.5% average strain. The largest damage is induced at the grain boundary between a grain with twins and a grain without twins. The propagation of the crack at the grain boundary between the two grains with twins is slower.

In order to better investigate the dynamics of the crack propagation, the damage variable D and the twin

variable φ are reported along the upper grain boundary (between grain 1 and 2) for texture 1. These two quantities are taken along a node path, as shown in Fig. 6b, and reported in the same plot at different values of the strain, as shown in Fig. 8. The discrete nature of the twinning process results in a non-uniform distribution of stress along the grain boundaries, with the stress normal to a boundary being greatest adjacent to

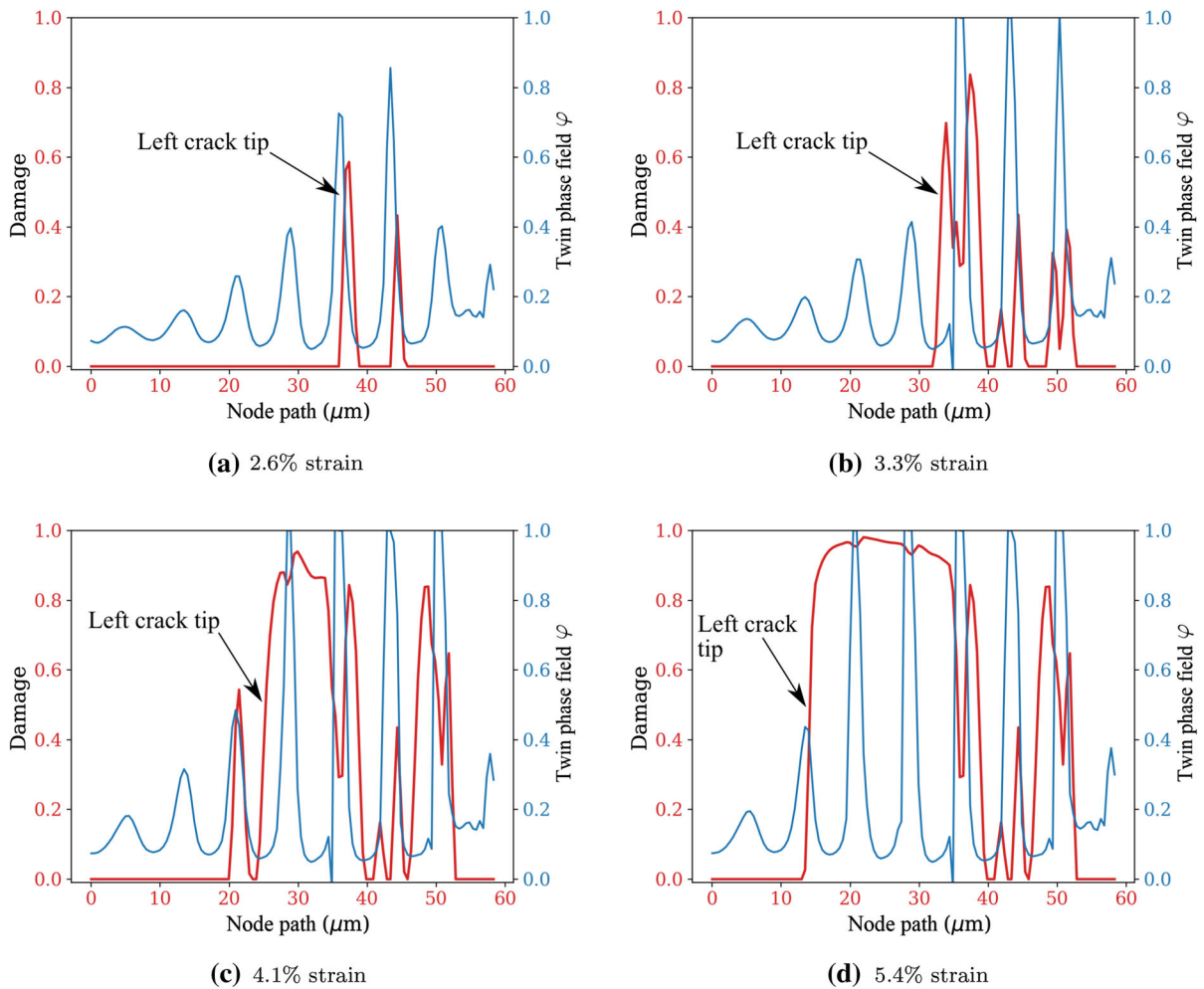


Fig. 8 Damage variable and twin variable φ along the node path in Fig. 6b for texture 1

a twin. Crack nucleation (Fig. 8a) takes place on the right side of a twin tip due to the tensile stress caused by twinning. Cracks nucleate at two points adjacent to two neighbouring twins independently. As the macroscopic strain is increased, and twinning intensifies, intergranular damage develops to the left of one of the twins, promoting the development of damage at the twin, leading to the formation of a crack that propagates towards the next twin (labelled left crack tip in Fig. 8b). Other cracks nucleate ahead of this crack tip as other twins reach the grain boundary (Fig. 8c), which merge with the propagating crack. The motion of the left crack tip slows down when it meets a nucleating twin (Fig. 8d). The interaction with a twin nucleus also speeds up the nucleation and growth of the twin because of the stress concentration induced.

Figure 9a shows the position of the left and right crack tips in Fig. 8 as a function of time. Their positions are calculated as follows. The position of the crack tip is initialised where the crack first nucleates. At each time increment, an algorithm searches to the left and right of the current crack tip positions. The new crack tip positions are defined as the last node found by the algorithm at which $D > 0.5$. Figure 9a reports also the crack tip positions for texture 2.

As shown in Fig. 9a, the crack tip position does not increase uniformly with time. As discussed previously, the crack at the upper grain boundary in texture 1 tends to propagate towards the left. Therefore, Fig. 9a shows a larger motion of that left crack tip. The right crack tip in texture 1 advances at the beginning, but then its position remains almost stationary for the rest of the

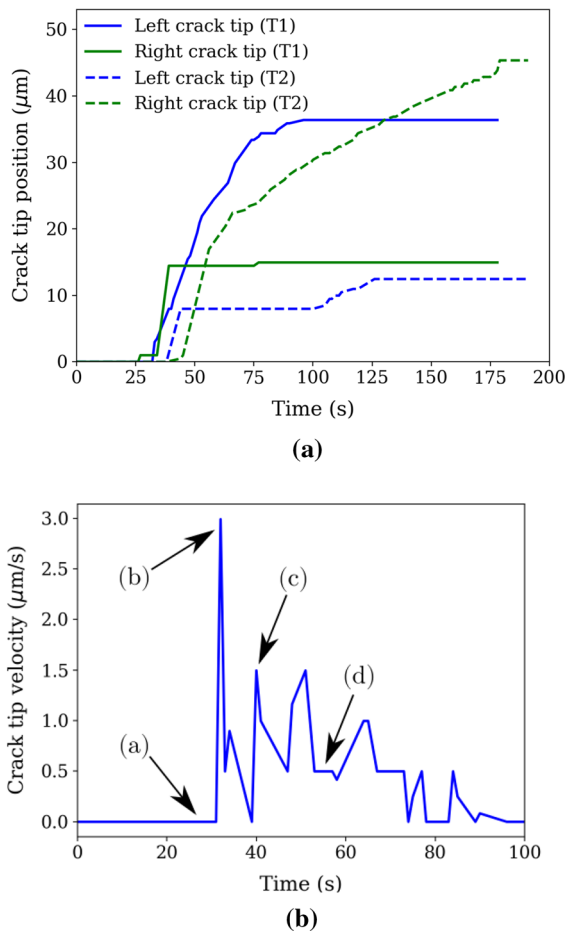


Fig. 9 **a** Crack tip propagation along the upper grain boundary and **b** the velocity of the left crack tip of texture 1 in Fig. 7a

simulation. This is due to plastic relaxation due to the presence of twins on both sides of the grain boundaries and to the rotation of grains 1 and 2. This rotation accommodates the tensile load on the top surface without further propagation of the crack towards the right.

The right crack tip in texture 2 propagates more uniformly, as shown in Fig. 9a. This is because this crack tip does not interact with any twin during its motion, as shown in Fig. 7b.

Figure 9b shows the left crack tip velocity in texture 1, i.e. the time derivative of the left crack tip position. The arrows (a), (b), (c), (d) correspond to the values of the average strain in Fig. 8. Velocity peaks are present when the crack tip propagates between two twin tips, while the velocity has minima whenever the crack tip meets a twin tip or a nucleating twin.

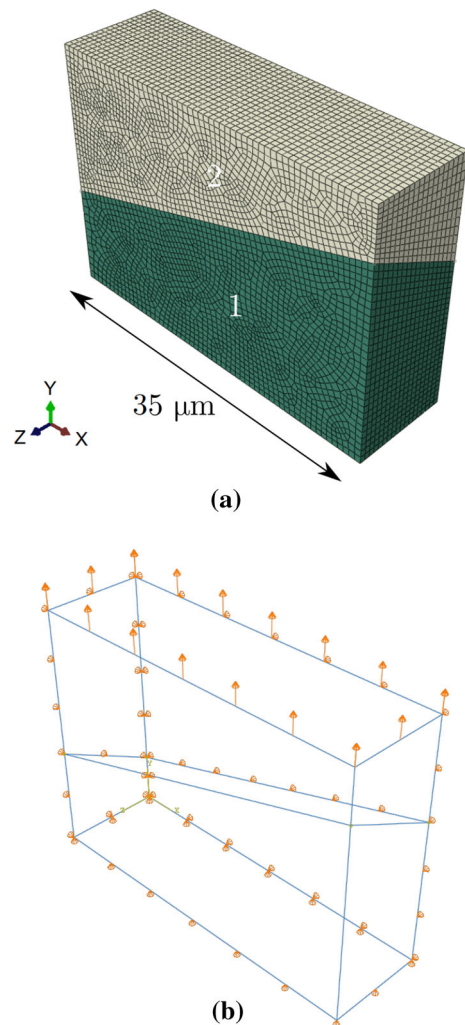


Fig. 10 3D non-columnar bicrystal: **a** mesh and **b** boundary conditions

6 Bicrystal simulation with non-columnar grains

All the previous simulations were carried out using columnar grains. A bicrystal representative volume with two non-columnar grains is investigated to understand the effect of discrete twins on intergranular fracture for the case in which the grain boundary surface normal is not coplanar with both the twin direction and twin plane normal.

The representative volume and mesh are shown in Fig. 10a. Figure 10b shows only the edges of the two grains and clarifies the orientation of the grain boundary. The size of the representative volume is 35 μm

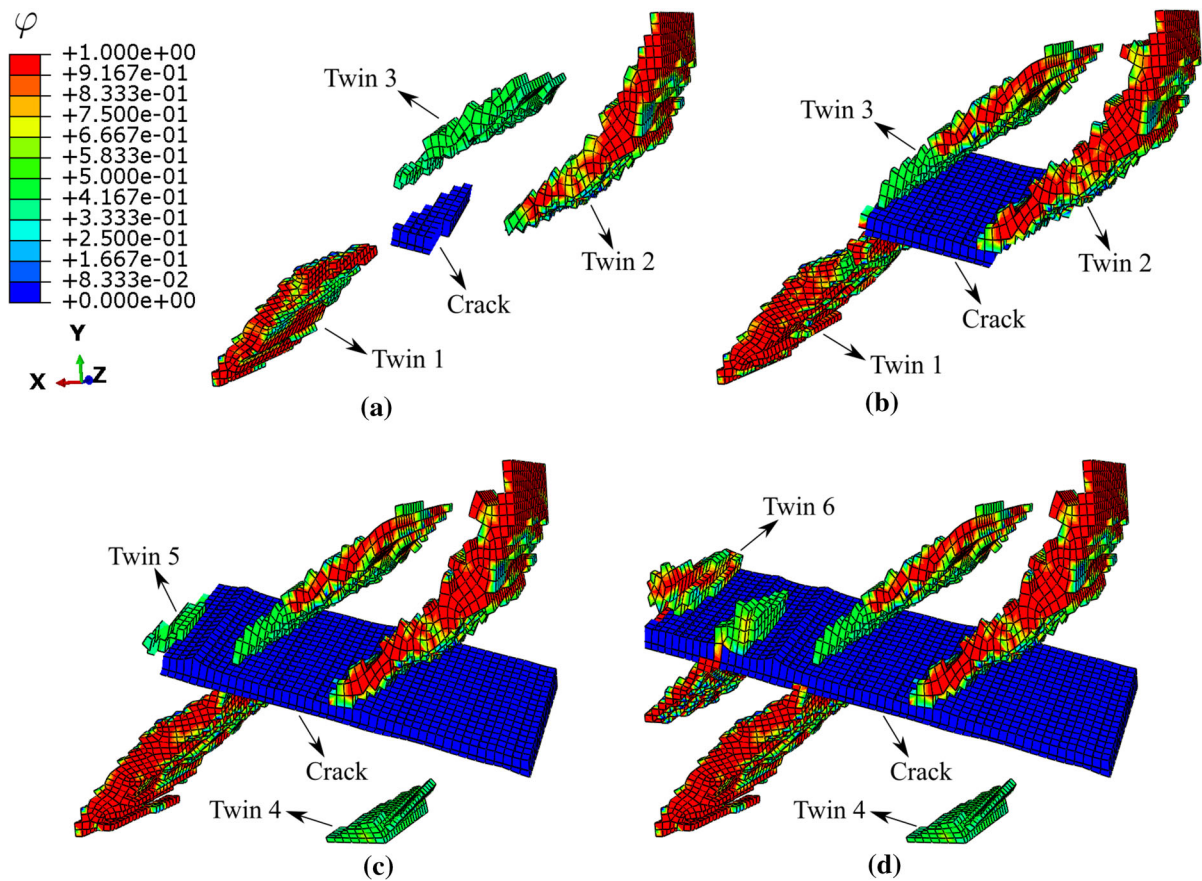


Fig. 11 Bicrystal simulation with non-columnar grains: twin variable φ and damaged plane (blue). Only larger twins with elements in which $\varphi > 0.4$ are shown. The crack is constituted of elements with $D > 0.9$. **a** 18%, **b** 23%, **c** 30%, **d** 38% strain

$\times 25 \mu\text{m} \times 10 \mu\text{m}$. The mesh consists of hexahedral elements with average size $0.6 \mu\text{m}$.

Boundary conditions for pure tension are shown in Fig. 10b. $u_z = 0$ is imposed on the surface $z = 0$, $u_y = 0$ is imposed on the surface $y = 0$, $u_x = 0$ is imposed on the surface $x = 0$. A displacement u_y is imposed on the surface $y = 25 \mu\text{m}$. This displacement increases linearly with time.

The orientation of the crystal lattice of grains 1 and 2 in Fig. 10a is:

$$\mathbf{R}_1 = \begin{pmatrix} -0.1834 & 0.983 & 0 \\ 0.983 & 0.1834 & 0 \\ 0 & 0 & -1 \end{pmatrix}, \quad (23)$$

$$\mathbf{R}_2 = \begin{pmatrix} -0.3513 & 0.9362 & 0 \\ 0.9362 & 0.3513 & 0 \\ 0 & 0 & -1 \end{pmatrix}. \quad (24)$$

Since the grain boundary is almost perpendicular to the load direction, the maximum stress of the interface elements has been increased to $\sigma_{\text{max}} = 800 \text{ MPa}$ in order to observe the complete development of discrete twins before failure.

The time evolution of the twin variable φ is shown in Fig. 11. The main discrete twins, consisting of at least 50 elements with $\varphi > 0.4$, are shown and numbered. The blue region represents the crack, i.e. the surface of the grain boundary on which $D > 0.9$.

Twins 1 and 2 are the largest discrete twins, which nucleate in the central part of the geometry on different planes. They therefore impinge on the grain boundary at two different locations. The tensile stress induced by twins 1 and 2 on the grain boundary is maximum between the two twin tips, and a crack first nucleates here (Fig. 11a). The crack nucleates near the surface $z = 0$. This is due to the orientation of the grain bound-

ary: the tip of twin 1, which is the most important in determining crack nucleation, is closer to the grain boundary on the surface $z = 0$ than on the surface $z = 10 \mu\text{m}$. The fracture plane propagates first along the direction parallel to the twin plane, then along the grain boundary (Fig. 11b). The damage surface propagates much faster towards the right (Fig. 11c). This is because twin 2 is already completely formed when the crack propagates near its tip, while the nucleation of twin 5 at the crack tip slows down its propagation (Fig. 11c). The stress is not high enough to propagate twin 4, because the grain boundary above it is completely damaged. The stress concentration induced by the left crack tip leads to the nucleation and propagation of twin 5 before the grain boundary is completely damaged (Fig. 11d).

7 Discussion

The model calibration carried out in Sect. 4 shows that the knowledge of a lower bound on the maximum stress and the strain to failure is sufficient to precisely calibrate the parameter σ_{max} of the cohesive zone model. This is due to the strong dependence of the strain to failure on σ_{max} in the coupled discrete twin-fracture model. This type of calibration has been used for mode I tearing of plates (Woelke et al. 2015). Models including void nucleation and growth are also calibrated using the experimental strain to failure (Perzyna 1984).

Since intergranular fracture depends mostly on the stress normal to the grain boundary interface (Simonovski and Cizelj 2011), the grain boundaries that are predicted to fail earlier are the ones perpendicular to the load direction.

The texture plays an important role on crack nucleation and propagation, as shown in Sect. 5. If two neighbouring grains have similar orientations, the stress concentration at the grain boundary induced by twin tips in one grain is relaxed by twins in the neighbouring grains. If a grain boundary has one neighbouring grain that twins and another neighbouring grain that does not twin, stress relaxation cannot take place. In this case, failure of the grain boundary is faster. This behaviour is similar to brittle materials with highly oriented microstructures, in which the fracture toughness approaches that of a single crystal (Schultz et al. 1994). It is also consistent with the experimental results on TiAl (Bieler et al. 2005), in which the weaker grain

boundaries are the ones in which the neighbouring grain cannot accommodate the twin strain.

The present simulations reveal an additional effect of the texture. As shown in Figs. 7b and 11, a propagating crack can prevent the growth of twins in grains that are favourably oriented for twinning. This happens if the deformation can be accommodated by other mechanisms, such as grain rotation in Fig. 7b, or if the grain boundary is almost perpendicular to the load direction (twin 4 in Fig. 11).

The present simulations clarify the chronological order of twin and crack nucleation (Mahajan and Williams 1973). Twins nucleate first. Once a twin impinges on a grain boundary, the tensile stress that is present on one side of the twin tip is sufficient to nucleate a crack. The crack first propagates along a direction parallel to the twin plane until the intersection between the twin tip and the twin plane is completely damaged. Then, the crack propagates along the grain boundary, as shown in Sect. 6. If multiple twins impinge on the same grain boundary, multiple microcracks can nucleate in correspondence to the different twin tips and then merge, as shown in Sect. 5. The propagating crack can induce stress concentrations that are sufficient to nucleate a twin starting from the grain boundary. Patterns of twins extending from the grain boundaries towards the centre of the grains are commonly observed (Gusse et al. 2018). The stress relaxation induced by the nucleation of these twins slows down the propagation of the crack tip.

In the crystal plasticity model used, dislocation slip is present in both the twinned and untwinned regions. The simulations show crack nucleation near twin tips and there is no strong correlation with slip, which is a more uniform plastic deformation mode in the simulated grains. The stored dislocation energy density has been identified as an important factor to explain the locations of the observed twins (Paramatmuni et al. 2020), but in the present simulations the dislocation density does not affect the critical stress for twin nucleation. Including slip bands in the present model would be necessary to describe metals in which twin-induced microcracks are observed, while the actual failure is slip-induced (Reid 1981).

Twin boundary cracking (twin parting) is another observed fracture mechanism that we have not specifically investigated in this paper (Cahn 1953; McCabe et al. 2008).

8 Conclusions

In this paper, we have coupled a discrete twin model and a cohesive zone model to understand the effect of the stress induced by twins on intergranular fracture. The dynamics of twin-induced intergranular fracture is clarified. Microcracks nucleate near the intersection between a twin tip and a grain boundary, in the area where the twin tip induces a high tensile stress. The subsequent crack propagation can nucleate more twins, which then propagate away from the grain boundary. This mechanism slows down crack propagation. Therefore, a grain boundary, surrounded by two grains that are favourably oriented for twinning, is more resistant against fracture.

An algorithm that can generate the interface elements along grain boundaries of arbitrary polycrystals has been developed. This model can be used to predict the strain to failure and stress–strain curve of cast metals, given the specific orientation of the grains.

Acknowledgements The authors acknowledge financial support from AWE plc for this research, program manager: Dr John Askew. ET acknowledges support from the Engineering and Physical Sciences Research Council under Fellowship grant EP/N007239/1.

Open Access This article is licensed under a Creative Commons Attribution 4.0 International License, which permits use, sharing, adaptation, distribution and reproduction in any medium or format, as long as you give appropriate credit to the original author(s) and the source, provide a link to the Creative Commons licence, and indicate if changes were made. The images or other third party material in this article are included in the article's Creative Commons licence, unless indicated otherwise in a credit line to the material. If material is not included in the article's Creative Commons licence and your intended use is not permitted by statutory regulation or exceeds the permitted use, you will need to obtain permission directly from the copyright holder. To view a copy of this licence, visit <http://creativecommons.org/licenses/by/4.0/>.

Appendix A: Shape functions of the cohesive element

The separation vector $\mathbf{\Delta} = (\Delta_{s1}, \Delta_{s2}, \Delta_n)$, expressed in the mid-plane reference frame, is a function of the coordinates on the $(\hat{\mathbf{x}}_m, \hat{\mathbf{y}}_m)$ plane. Given the deformed coordinates of the nodes $\mathbf{x}_1, \mathbf{x}_2, \mathbf{x}_3, \mathbf{x}_4, \mathbf{x}_5, \mathbf{x}_6, \mathbf{x}_7, \mathbf{x}_8$ of the cohesive element in Fig. 1, the separation vectors at the mid-points m1, m2, m3, m4 are given by:

$$\mathbf{\Delta}_{m1} = \mathbf{x}_5 - \mathbf{x}_1 = \mathbf{u}_5 - \mathbf{u}_1, \quad (9.1)$$

Table 4 Coordinates of the Gauss points of the cohesive elements in the reference square element

GP1	$\xi_1 = -1/\sqrt{3}$	$\eta_1 = -1/\sqrt{3}$
GP2	$\xi_2 = 1/\sqrt{3}$	$\eta_2 = -1/\sqrt{3}$
GP3	$\xi_3 = 1/\sqrt{3}$	$\eta_3 = 1/\sqrt{3}$
GP4	$\xi_4 = -1/\sqrt{3}$	$\eta_4 = 1/\sqrt{3}$

$$\mathbf{\Delta}_{m2} = \mathbf{x}_6 - \mathbf{x}_2 = \mathbf{u}_6 - \mathbf{u}_2, \quad (9.2)$$

$$\mathbf{\Delta}_{m3} = \mathbf{x}_7 - \mathbf{x}_3 = \mathbf{u}_7 - \mathbf{u}_3, \quad (9.3)$$

$$\mathbf{\Delta}_{m4} = \mathbf{x}_8 - \mathbf{x}_4 = \mathbf{u}_8 - \mathbf{u}_4. \quad (9.4)$$

These separation vectors can be expressed also as a function of the displacement vectors of the nodes $\mathbf{u}_1, \mathbf{u}_2, \mathbf{u}_3, \mathbf{u}_4, \mathbf{u}_5, \mathbf{u}_6, \mathbf{u}_7, \mathbf{u}_8$ because nodes in the pairs (1, 5), (2, 6), (3, 7), (4, 8) are coincident in the undeformed configuration.

Four shape functions are used to interpolate the separation vector on the $(\hat{\mathbf{x}}_m, \hat{\mathbf{y}}_m)$ plane (Cook 1995):

$$\phi_1(\xi, \eta) = \frac{1}{4}(1 - \xi)(1 - \eta), \quad (9.5)$$

$$\phi_2(\xi, \eta) = \frac{1}{4}(1 + \xi)(1 - \eta), \quad (9.6)$$

$$\phi_3(\xi, \eta) = \frac{1}{4}(1 + \xi)(1 + \eta), \quad (9.7)$$

$$\phi_4(\xi, \eta) = \frac{1}{4}(1 - \xi)(1 + \eta), \quad (9.8)$$

where $-1 < \xi < 1$, $-1 < \eta < 1$ are the coordinate of a reference square element. Therefore, the separation vector can be written as:

$$\mathbf{\Delta} = \phi_1 \mathbf{\Delta}_{m1} + \phi_2 \mathbf{\Delta}_{m2} + \phi_3 \mathbf{\Delta}_{m3} + \phi_4 \mathbf{\Delta}_{m4}. \quad (9.9)$$

Eqs. (9.1)–(9.4) and (9.9) are linear relationships between the separation vector and the displacement vectors of the nodes. Therefore, it is possible to build a $[24 \times 1]$ vector:

$$\mathbf{U} = (\mathbf{u}_1, \mathbf{u}_2, \mathbf{u}_3, \mathbf{u}_4, \mathbf{u}_5, \mathbf{u}_6, \mathbf{u}_7, \mathbf{u}_8)^T \quad (9.10)$$

which contains the three displacement components of the eight nodes, and to define a $[3 \times 24]$ matrix \mathbf{B} such that (Alfano et al. 2015):

$$\mathbf{\Delta} = \mathbf{B}\mathbf{U} . \tag{9. 11}$$

The \mathbf{B} matrix is a function of the coordinates (ξ, η) .

Four Gauss points are used for the calculation of the internal force vector in Eq. (9). Their coordinates in the reference element are reported in Table 4.

Appendix B: Jacobian calculation

The Jacobian contribution of one cohesive element Γ_e is found by calculating the derivative of \mathbf{f}_{coh}^e in Eq. (9) with respect to the nodal displacement vector \mathbf{U}_G :

$$\frac{\partial \mathbf{f}_{coh}^e}{\partial \mathbf{U}_G} = \int_{\Gamma_e} \mathbf{M}^T \mathbf{B}^T \frac{\partial \mathbf{T}}{\partial \mathbf{U}_G} dS . \tag{10. 1}$$

The derivative of the rotation matrices in \mathbf{M} are neglected to increase the computational efficiency. This Jacobian leads to good convergence if no rigid body rotations are applied to the representative volume. Using the relationship between the separation vector $\mathbf{\Delta}$ and the nodal displacement vector \mathbf{U}_G :

$$\mathbf{\Delta} = \mathbf{B}\mathbf{M}\mathbf{U}_G , \tag{10. 2}$$

Eq. (10. 1) becomes:

$$\frac{\partial \mathbf{f}_{coh}^e}{\partial \mathbf{U}_G} = \int_{\Gamma_e} \mathbf{M}^T \mathbf{B}^T \frac{\partial \mathbf{T}}{\partial \mathbf{\Delta}} \frac{\partial \mathbf{\Delta}}{\partial \mathbf{U}_G} dS = \int_{\Gamma_e} \mathbf{M}^T \mathbf{B}^T \frac{\partial \mathbf{T}}{\partial \mathbf{\Delta}} \mathbf{B}\mathbf{M} dS \tag{10. 3}$$

which is a non-symmetric $[24 \times 24]$ matrix due to the lack of symmetry in $\partial \mathbf{T} / \partial \mathbf{\Delta}$. Therefore the unsymmetric solver option is specified in the Abaqus input file (Smith 2009). The integral is evaluated using the four Gauss points of the cohesive element.

The Jacobian in the mid-plane reference frame $\partial \mathbf{T} / \partial \mathbf{\Delta}$ is a $[3 \times 3]$ matrix that is obtained from the derivatives of the traction vector components in Eqs. (2)–(5):

$$\frac{\partial T_n}{\partial \Delta_n} = \begin{cases} K_n, & \text{if } D = 0 \text{ or } \Delta_n < 0, \\ 0, & \text{if } D = 1 \text{ and } \Delta_n > 0, \\ K_n (1 - D), & \text{if } 0 < D < 1 \text{ and } 0 < \Delta_n < \Delta_p(D), \\ -K_n \frac{\Delta_0}{(\Delta_f - \Delta_0)}, & \text{if } 0 < D < 1 \text{ and } \Delta_n > \Delta_p(D) . \end{cases} \tag{10. 4}$$

$$\frac{\partial T_s}{\partial \Delta_s} = \begin{cases} G_s, & \text{if } D = 0, \\ 0, & \text{if } D = 1, \\ G_s (1 - D), & \text{if } 0 < D < 1 . \end{cases} \tag{10. 5}$$

The derivatives along the two shear components can be found as:

$$\begin{aligned} \frac{\partial T_{s1}}{\partial \Delta_{s1}} &= \frac{\partial T_s}{\partial \Delta_{s1}} \frac{\Delta_{s1}}{\Delta_s} + T_s \frac{\partial}{\partial \Delta_{s1}} \left(\frac{\Delta_{s1}}{\Delta_s} \right) \\ &= \frac{\partial T_s}{\partial \Delta_s} \frac{\Delta_{s1}^2}{\Delta_s^2} + T_s \left(\frac{\Delta_{s1}^2}{\Delta_s^3} \right), \end{aligned} \tag{10. 6}$$

$$\begin{aligned} \frac{\partial T_{s2}}{\partial \Delta_{s2}} &= \frac{\partial T_s}{\partial \Delta_{s2}} \frac{\Delta_{s2}}{\Delta_s} + T_s \frac{\partial}{\partial \Delta_{s2}} \left(\frac{\Delta_{s2}}{\Delta_s} \right) \\ &= \frac{\partial T_s}{\partial \Delta_s} \frac{\Delta_{s2}^2}{\Delta_s^2} + T_s \left(\frac{\Delta_{s2}^2}{\Delta_s^3} \right), \end{aligned} \tag{10. 7}$$

$$\begin{aligned} \frac{\partial T_{s1}}{\partial \Delta_{s2}} &= \frac{\partial T_s}{\partial \Delta_{s2}} \frac{\Delta_{s1}}{\Delta_s} + T_s \frac{\partial}{\partial \Delta_{s2}} \left(\frac{\Delta_{s1}}{\Delta_s} \right) \\ &= \frac{\partial T_s}{\partial \Delta_s} \frac{\Delta_{s1} \Delta_{s2}}{\Delta_s^2} - T_s \left(\frac{\Delta_{s1} \Delta_{s2}}{\Delta_s^3} \right), \end{aligned} \tag{10. 8}$$

$$\begin{aligned} \frac{\partial T_{s2}}{\partial \Delta_{s1}} &= \frac{\partial T_s}{\partial \Delta_{s1}} \frac{\Delta_{s2}}{\Delta_s} + T_s \frac{\partial}{\partial \Delta_{s1}} \left(\frac{\Delta_{s2}}{\Delta_s} \right) \\ &= \frac{\partial T_s}{\partial \Delta_s} \frac{\Delta_{s1} \Delta_{s2}}{\Delta_s^2} - T_s \left(\frac{\Delta_{s1} \Delta_{s2}}{\Delta_s^3} \right) . \end{aligned} \tag{10. 9}$$

The off-diagonal derivatives, i.e. derivatives of the normal traction with respect to shear separation and vice-versa, are not all zero because an increase of normal displacement leads to an increase in the damage and consequent decrease of the shear traction:

$$\frac{\partial T_n}{\partial \Delta_{s1}} = 0, \tag{10. 10}$$

$$\frac{\partial T_n}{\partial \Delta_{s2}} = 0, \tag{10. 11}$$

$$\frac{\partial T_{s1}}{\partial \Delta_n} = \frac{\partial T_s}{\partial \Delta_n} \frac{\Delta_{s1}}{\Delta_s}, \tag{10. 12}$$

$$\frac{\partial T_{s2}}{\partial \Delta_n} = \frac{\partial T_s}{\partial \Delta_n} \frac{\Delta_{s2}}{\Delta_s} . \tag{10. 13}$$

If Δ_n is increasing and $\Delta_n > \Delta_p$, then damage increases, otherwise the damage variable is constant:

$$D(\Delta_n) = \begin{cases} \frac{\Delta_f (\Delta_n - \Delta_0)}{\Delta_n (\Delta_f - \Delta_0)}, & \text{if } \Delta_p < \Delta_n < \Delta_f, \\ \frac{\Delta_f (\Delta_p - \Delta_0)}{\Delta_p (\Delta_f - \Delta_0)}, & \text{if } \Delta_n < \Delta_p, \\ 1, & \text{if } \Delta_n > \Delta_f . \end{cases} \tag{10. 14}$$

Therefore, the derivative of the shear traction with respect to the normal displacement are found from Eq. (3):

$$\frac{\partial T_s}{\partial \Delta_n} = \begin{cases} -G_s \frac{\partial D(\Delta_n)}{\partial \Delta_n} \Delta_s = -G_s \frac{\Delta_f \Delta_0 \Delta_s}{\Delta_n^2 (\Delta_f - \Delta_0)}, & \text{if } \Delta_p < \Delta_n < \Delta_f, \\ 0, & \text{otherwise.} \end{cases} \quad (10.15)$$

References

- Abdolvand H, Wilkinson AJ (2016) Assessment of residual stress fields at deformation twin tips and the surrounding environments. *Acta Mater* 105:219–231. <https://doi.org/10.1016/j.actamat.2015.11.036>
- Alfano M, Lubineau G, Paulino GH (2015) Global sensitivity analysis in the identification of cohesive models using full-field kinematic data. *Int J Solids Struct* 55:66–78. <https://doi.org/10.1016/j.ijsolstr.2014.06.006>. Special issue computational and experimental mechanics of advanced materials a workshop held at King Abdullah University of Science and Technology Jeddah, Kingdom of Saudi Arabia July 1–3, 2013
- Balogh L, Niezgodá S, Kanjarla A, Brown D, Clausen B, Liu W, Tomé C (2013) Spatially resolved in situ strain measurements from an interior twinned grain in bulk polycrystalline az31 alloy. *Acta Mater* 61(10):3612–3620. <https://doi.org/10.1016/j.actamat.2013.02.048>
- Barenblatt G (1962) The mathematical theory of equilibrium cracks in brittle fracture. *Adv Appl Mech* 7:55–129. [https://doi.org/10.1016/S0065-2156\(08\)70121-2](https://doi.org/10.1016/S0065-2156(08)70121-2)
- Barrera O, Bombac D, Chen Y, Daff TD, Galindo-Nava E, Gong P, Haley D, Horton R, Katarov I, Kermode JR, Liverani C, Stopher M, Sweeney F (2018) Understanding and mitigating hydrogen embrittlement of steels: a review of experimental, modelling and design progress from atomistic to continuum. *J Mater Sci* 53(9):6251–6290. <https://doi.org/10.1007/s10853-017-1978-5>
- Beyerlein I, Tomé C (2008) A dislocation-based constitutive law for pure Zr including temperature effects. *Int J Plast* 24(5):867–895. <https://doi.org/10.1016/j.ijplas.2007.07.017>
- Bieler T, Fallahi A, Ng B, Kumar D, Crimp M, Simkin B, Zamiri A, Pourboghrat F, Mason D (2005) Fracture initiation/propagation parameters for duplex tial grain boundaries based on twinning, slip, crystal orientation, and boundary misorientation. 2nd IRC international TiAl workshop. *Intermetallics* 13(9):979–984. <https://doi.org/10.1016/j.intermet.2004.12.013>
- Birbilis N, Hinton B (2011) 19-Corrosion and corrosion protection of aluminium. In: Lumley R (ed) *Fundamentals of aluminium metallurgy*. Woodhead Publishing Series in Metals and Surface Engineering. Woodhead Publishing, Cambridge, pp 574–604
- Boucher N, Christian J (1972) The influence of pre-strain on deformation twinning in niobium single crystals. *Acta Metall* 20(4):581–591. [https://doi.org/10.1016/0001-6160\(72\)90013-2](https://doi.org/10.1016/0001-6160(72)90013-2)
- Cahn R (1953) Plastic deformation of alpha-uranium; twinning and slip. *Acta Metall* 1(1):49–70. [https://doi.org/10.1016/0001-6160\(53\)90009-1](https://doi.org/10.1016/0001-6160(53)90009-1)
- Camacho G, Ortiz M (1996) Computational modelling of impact damage in brittle materials. *Int J Solids Struct* 33(20):2899–2938. [https://doi.org/10.1016/0020-7683\(95\)00255-3](https://doi.org/10.1016/0020-7683(95)00255-3)
- Chen W, Ravichandran G (1996) Static and dynamic compressive behavior of aluminum nitride under moderate confinement. *J Am Ceram Soc* 79(3):579–584. <https://doi.org/10.1111/j.1151-2916.1996.tb07913.x>
- Chen W, Ravichandran G (1997) Dynamic compressive failure of a glass ceramic under lateral confinement. *J Mech Phys Solids* 45(8):1303–1328. [https://doi.org/10.1016/S0022-5096\(97\)00006-9](https://doi.org/10.1016/S0022-5096(97)00006-9)
- Cheng J, Shahba A, Ghosh S (2016) Stabilized tetrahedral elements for crystal plasticity finite element analysis overcoming volumetric locking. *Comput Mech* 57:733–753. <https://doi.org/10.1007/s00466-016-1258-2>
- Christian J (2002) Chapter 20-Deformation twinning. In: Christian J (ed) *The theory of transformations in metals and alloys*. Pergamon, Oxford, pp 859–960
- Christian J, Mahajan S (1995) Deformation twinning. *Progr Mater Sci* 39(1):1–157. [https://doi.org/10.1016/0079-6425\(94\)00007-7](https://doi.org/10.1016/0079-6425(94)00007-7)
- Chun JS, Byrne JG, Bornemann A (1969) The inhibition of deformation twinning by precipitates in a magnesium-zinc alloy. *Philos Mag* 20(164):291–300. <https://doi.org/10.1080/14786436908228701>
- Clayton J, Knap J (2016) Phase field modeling and simulation of coupled fracture and twinning in single crystals and polycrystals, phase field approaches to fracture. *Comput Methods Appl Mech Eng* 312:447–467. <https://doi.org/10.1016/j.cma.2016.01.023>
- Cocks A, Ashby M (1982) On creep fracture by void growth. *Progr Mater Sci* 27(3):189–244. [https://doi.org/10.1016/0079-6425\(82\)90001-9](https://doi.org/10.1016/0079-6425(82)90001-9)
- Collins A, Taplin D (1978) An experimental fracture map for uranium. *J Mater Sci* 13:2249–2256. <https://doi.org/10.1007/BF00541681>
- Cook RD (1995) *Finite element modeling for stress analysis*. Wiley, New York
- Davies D, Martin J (1961) The effect of inclusions on the fracture of uranium. *J Nucl Mater* 3(2):156–161. [https://doi.org/10.1016/0022-3115\(61\)90003-4](https://doi.org/10.1016/0022-3115(61)90003-4)
- Duarte CA, Grilli N, Koslowski M (2018) Effect of initial damage variability on hot-spot nucleation in energetic materials. *J Appl Phys* 124(2):025104. <https://doi.org/10.1063/1.5030656>
- Dunne F, Petrinic N (2006) *Introduction to computational plasticity*. Oxford University Press, Oxford
- Dunne F, Rugg D, Walker A (2007) Lengthscale-dependent, elastically anisotropic, physically-based hcp crystal plasticity: application to cold-dwell fatigue in Ti alloys. *Int J Plast* 23(6):1061–1083. <https://doi.org/10.1016/j.ijplas.2006.10.013>
- Earp P, Kabra S, Askew J, Marrow TJ (2018) Lattice strain and texture development in coarse-grained uranium—a neutron diffraction study. *J Phys* 1106:012012. <https://doi.org/10.1088/1742-6596/1106/1/012012>
- Elmukashfi E, Tarleton E, Cocks ACF (2020) A modelling framework for coupled hydrogen diffusion and mechanical

- behaviour of engineering components. *Comput Mech* 66:189–220. <https://doi.org/10.1007/s00466-020-01847-9>
- Fisher ES, McSkimin HJ (1958) Adiabatic elastic moduli of single crystal alpha uranium. *J Appl Phys* 29(10):1473–1484. <https://doi.org/10.1063/1.1722972>
- Frøseth AG, Derlet PM, Van Swygenhoven H (2005) Twinning in nanocrystalline fcc metals. *Adv Eng Mater* 7(1–2):16–20. <https://doi.org/10.1002/adem.200400163>
- Gilbert A, Hahn G, Reid C, Wilcox B (1964) Twin-induced grain boundary cracking in bcc metals. *Acta Metall* 12(6):754–755. [https://doi.org/10.1016/0001-6160\(64\)90230-5](https://doi.org/10.1016/0001-6160(64)90230-5)
- Gong M, Liu G, Wang J, Capolungo L, Tomé CN (2018) Atomistic simulations of interaction between basal α_2 dislocations and three-dimensional twins in magnesium. *Acta Mater* 155:187–198. <https://doi.org/10.1016/j.actamat.2018.05.066>
- Grilli N (2016) Physics-based constitutive modelling for crystal plasticity finite element computation of cyclic plasticity in fatigue. PhD thesis, École Polytechnique Fédérale de Lausanne, 10.5075/epfl-thesis-7251, <https://infoscience.epfl.ch/record/223625>
- Grilli N (2020) PyCiGen. <https://github.com/ngrilli/PyCiGen>
- Grilli N, Tarleton E, Cocks (2021) ACF Neper2CAE and PyCiGen: scripts to generate polycrystals and interface elements in Abaqus. SoftwareX (in press)
- Grilli N, Koslowski M (2018) The effect of crystal orientation on shock loading of single crystal energetic materials. *Comput Mater Sci* 155:235–245. <https://doi.org/10.1016/j.commatsci.2018.08.059>
- Grilli N, Koslowski M (2019) The effect of crystal anisotropy and plastic response on the dynamic fracture of energetic materials. *J Appl Phys* 126(15):155101. <https://doi.org/10.1063/1.5109761>
- Grilli N, Janssens KG, Swygenhoven HV (2015) Crystal plasticity finite element modelling of low cycle fatigue in fcc metals. *J Mech Phys Solids* 84:424–435. <https://doi.org/10.1016/j.jmps.2015.08.007>
- Grilli N, Duarte CA, Koslowski M (2018a) Dynamic fracture and hot-spot modeling in energetic composites. *J Appl Phys* 123(6):065101. <https://doi.org/10.1063/1.5009297>
- Grilli N, Janssens K, Nellessen J, Sandlöbes S, Raabe D (2018b) Multiple slip dislocation patterning in a dislocation-based crystal plasticity finite element method. *Int J Plast* 100:104–121. <https://doi.org/10.1016/j.ijplas.2017.09.015>
- Grilli N, Cocks A (2019) Tarleton E (2019) Crystal plasticity finite element simulations of cast α -uranium. In: Onate E, Owen D, Peric D, Chiumenti M (eds) *Computational plasticity XV: fundamentals and applications*, 15th International conference on computational plasticity—fundamentals and applications (COMPLAS). Spain, Sep, Barcelona, pp 03–05
- Grilli N, Cocks AC, Tarleton E (2020a) Crystal plasticity finite element modelling of coarse-grained α -uranium. *Comput Mater Sci* 171:109276. <https://doi.org/10.1016/j.commatsci.2019.109276>
- Grilli N, Cocks AC, Tarleton E (2020b) A phase field model for the growth and characteristic thickness of deformation-induced twins. *J Mech Phys Solids* 143:104061. <https://doi.org/10.1016/j.jmps.2020.104061>
- Grilli N, Earp P, Cocks AC, Marrow J, Tarleton E (2020c) Characterisation of slip and twin activity using digital image correlation and crystal plasticity finite element simulation: application to orthorhombic α -uranium. *J Mech Phys Solids* 135:103800. <https://doi.org/10.1016/j.jmps.2019.103800>
- Grilli N, Tarleton E, Edmondson PD, Gussev MN, Cocks ACF (2020d) In situ measurement and modelling of the growth and length scale of twins in α -uranium. *Phys Rev Mater* 4:043605. <https://doi.org/10.1103/PhysRevMaterials.4.043605>
- Gussev M, Edmondson P, Leonard K (2018) Beam current effect as a potential challenge in SEM-EBSD in situ tensile testing. *Mater Charact* 146:25–34. <https://doi.org/10.1016/j.matchar.2018.09.037>
- Hubbell J, Seltzer SM (1995) Tables of x-ray mass attenuation coefficients and mass energy-absorption coefficients 1 keV to 20 MeV for elements Z = 1 to 92 and 48 additional substances of dosimetric interest. NIST, Boulder
- Huddart J, Harding J, Bleasdale P (1980) The effect of strain rate on the tensile flow and fracture of α -uranium. *J Nucl Mater* 89(2):316–330. [https://doi.org/10.1016/0022-3115\(80\)90063-X](https://doi.org/10.1016/0022-3115(80)90063-X)
- Irastorza-Landa A, Van Swygenhoven H, Van Petegem S, Grilli N, Bollhalder A, Brandstetter S, Grolimund D (2016) Following dislocation patterning during fatigue. *Acta Mater* 112:184–193. <https://doi.org/10.1016/j.actamat.2016.04.011>
- Irastorza-Landa A, Grilli N, Swygenhoven HV (2017a) Effect of pre-existing immobile dislocations on the evolution of geometrically necessary dislocations during fatigue. *Model Simul Mater Sci Eng* 25(5):055010. <https://doi.org/10.1088/1361-651x/aa6e24>
- Irastorza-Landa A, Grilli N, Swygenhoven HV (2017b) Laue micro-diffraction and crystal plasticity finite element simulations to reveal a vein structure in fatigued Cu. *J Mech Phys Solids* 104:157–171. <https://doi.org/10.1016/j.jmps.2017.04.010>
- Jafari M, Jamshidian M, Ziaei-Rad S, Raabe D, Roters F (2017) Constitutive modeling of strain induced grain boundary migration via coupling crystal plasticity and phase-field methods. *Int J Plast* 99:19–42. <https://doi.org/10.1016/j.ijplas.2017.08.004>
- Jiang J, Britton TB, Wilkinson AJ (2015) Evolution of intragranular stresses and dislocation densities during cyclic deformation of polycrystalline copper. *Acta Mater* 94:193–204. <https://doi.org/10.1016/j.actamat.2015.04.031>
- Kalidindi SR (1998) Incorporation of deformation twinning in crystal plasticity models. *J Mech Phys Solids* 46(2):267–290. [https://doi.org/10.1016/S0022-5096\(97\)00051-3](https://doi.org/10.1016/S0022-5096(97)00051-3)
- Kocks U, Mecking H (2003) Physics and phenomenology of strain hardening: the fcc case. *Progr Mater Sci* 48(3):171–273. [https://doi.org/10.1016/S0079-6425\(02\)00003-8](https://doi.org/10.1016/S0079-6425(02)00003-8)
- Koyama M, Akiyama E, Tsuzaki K, Raabe D (2013) Hydrogen-assisted failure in a twinning-induced plasticity steel studied under in situ hydrogen charging by electron channeling contrast imaging. *Acta Mater* 61(12):4607–4618. <https://doi.org/10.1016/j.actamat.2013.04.030>
- Krupp U (2007) *Fatigue crack propagation in metals and alloys: microstructural aspects and modelling concepts*. Wiley, New York
- Li W, Bei H, Gao Y (2016) Effects of geometric factors and shear band patterns on notch sensitivity in bulk metallic glasses. *Intermetallics* 79:12–19. <https://doi.org/10.1016/j.intermet.2016.09.001>

- Liu C, Shanthraj P, Diehl M, Roters F, Dong S, Dong J, Ding W, Raabe D (2018) An integrated crystal plasticity phase field model for spatially resolved twin nucleation, propagation, and growth in hexagonal materials. *Int J Plast* 106:203–227. <https://doi.org/10.1016/j.ijplas.2018.03.009>
- Liu C, Shanthraj P, Robson J, Diehl M, Dong S, Dong J, Ding W, Raabe D (2019) On the interaction of precipitates and tensile twins in magnesium alloys. *Acta Mater* 178:146–162. <https://doi.org/10.1016/j.actamat.2019.07.046>
- Lynch P, Kunz M, Tamura N, Barnett M (2014) Time and spatial resolution of slip and twinning in a grain embedded within a magnesium polycrystal. *Acta Mater* 78:203–212. <https://doi.org/10.1016/j.actamat.2014.06.030>
- Mahajan S, Williams DF (1973) Deformation twinning in metals and alloys. *Int Metall Rev* 18(2):43–61. <https://doi.org/10.1179/imtr.1973.18.2.43>
- Marcinkowski M, Lipsitt H (1962) The plastic deformation of chromium at low temperatures. *Acta Metall* 10(2):95–111. [https://doi.org/10.1016/0001-6160\(62\)90055-X](https://doi.org/10.1016/0001-6160(62)90055-X)
- McCabe R, Field R, Brown D, Alexander D, Cady C (2008) Electron backscatter diffraction (ebstd) characterization of twinning related deformation and fracture in α -uranium. *Microsc Microanal* 14(S2):638–639. <https://doi.org/10.1017/S1431927608083554>
- McCabe R, Capolungo L, Marshall P, Cady C, Tomé C (2010) Deformation of wrought uranium: experiments and modeling. *Acta Mater* 58(16):5447–5459. <https://doi.org/10.1016/j.actamat.2010.06.021>
- Oberson PG, Ankem S (2005) Why twins do not grow at the speed of sound all the time. *Phys Rev Lett*. <https://doi.org/10.1103/PhysRevLett.95.165501>
- Ojha A, Sehitoglu H, Patriarca L, Maier H (2014) Twin migration in Fe-based bcc crystals: theory and experiments. *Philos Mag* 94(16):1816–1840. <https://doi.org/10.1080/14786435.2014.898123>
- O'Neill H (1926) Deformation lines in large and small crystals of ferrite. *Iron Steel Inst* 113:417–445
- Ortiz M, Pandolfi A (1999) Finite-deformation irreversible cohesive elements for three-dimensional crack-propagation analysis. *Int J Num Methods Eng* 44(9):1267–1282. [https://doi.org/10.1002/\(SICI\)1097-0207\(19990330\)44:9<1267::AID-NME486>3.0.CO;2-7](https://doi.org/10.1002/(SICI)1097-0207(19990330)44:9<1267::AID-NME486>3.0.CO;2-7)
- Paramatmuni C, Zheng Z, Rainforth WM, Dunne FP (2020) Twin nucleation and variant selection in mg alloys: an integrated crystal plasticity modelling and experimental approach. *Int J Plast* 135:102778. <https://doi.org/10.1016/j.ijplas.2020.102778>
- Park K, Paulino GH (2012) Computational implementation of the ppr potential-based cohesive model in abaqus: educational perspective. *Eng Fract Mech* 93:239–262. <https://doi.org/10.1016/j.engfracmech.2012.02.007>
- Perzyna P (1984) Constitutive modeling of dissipative solids for postcritical behavior and fracture. *J Eng Mater Technol* 106(4):410–419. <https://doi.org/10.1115/1.3225739>
- Petkov MP, Hu J, Tarleton E, Cocks AC (2019) Comparison of self-consistent and crystal plasticity Fe approaches for modelling the high-temperature deformation of 316h austenitic stainless steel. *Int J Solids Struct* 171:54–80. <https://doi.org/10.1016/j.ijsolstr.2019.05.006>
- Pippan R, Hohenwarter A (2016) The importance of fracture toughness in ultrafine and nanocrystalline bulk materials. *Mater Res Lett* 4(3):127–136. <https://doi.org/10.1080/21663831.2016.1166403>
- Powell GW (1994) The fractography of casting alloys. *Mater Charact* 33(3):275–293. [https://doi.org/10.1016/1044-5803\(94\)90048-5](https://doi.org/10.1016/1044-5803(94)90048-5)
- Qian G, Lei WS, Niffenegger M, González-Albuixech VF (2018) On the temperature independence of statistical model parameters for cleavage fracture in ferritic steels. *Philos Mag* 98(11):959–1004. <https://doi.org/10.1080/14786435.2018.1425011>
- Qiao H, Barnett M, Wu P (2016) Modeling of twin formation, propagation and growth in a Mg single crystal based on crystal plasticity finite element method. *Int J Plast* 86:70–92. <https://doi.org/10.1016/j.ijplas.2016.08.002>
- Reid CN (1981) The association of twinning and fracture in bcc metals. *Metall Trans A* 12(3):371–377. <https://doi.org/10.1007/BF02648534>
- Roters F (2011) Advanced material models for the crystal plasticity finite element method - Development of a general CPFEM framework. RWTH, Aachen
- Roters F, Diehl M, Shanthraj P, Eisenlohr P, Reuber C, Wong S, Maiti T, Ebrahimi A, Hochrainer T, Fabritius HO, Nikolov S, Friák M, Fujita N, Grilli N, Janssens K, Jia N, Kok P, Ma D, Meier F, Werner E, Stricker M, Weygand D, Raabe D (2018) DAMASK-the Düsseldorf advanced material simulation kit for modeling multi-physics crystal plasticity, thermal, and damage phenomena from the single crystal up to the component scale. *Comput Mater Sci*. <https://doi.org/10.1016/j.commatsci.2018.04.030>
- Sakano MN, Hamed A, Kober EM, Grilli N, Hamilton BW, Islam MM, Koslowski M, Strachan A (2020) Unsupervised learning-based multiscale model of thermochemistry in 1,3,5-trinitro-1,3,5-triazinane (rdx). *J Phys Chem A* 124:9141–9155. <https://doi.org/10.1021/acs.jpca.0c07320>
- Sauzay M, Moussa MO (2013) Prediction of grain boundary stress fields and microcrack initiation induced by slip band impingement. *Int J Fract* 184:215–240. <https://doi.org/10.1007/s10704-013-9878-4>
- Schultz RA, Jensen MC, Bradt RC (1994) Single crystal cleavage of brittle materials. *Int J Fract* 65(4):291–312. <https://doi.org/10.1007/BF00012370>
- Simonovski I, Cizelj L (2011) Computational multiscale modeling of intergranular cracking. *J Nucl Mater* 414(2):243–250. <https://doi.org/10.1016/j.jnucmat.2011.03.051>
- Sistaninia M, Niffenegger M (2015) Fatigue crack initiation and crystallographic growth in 316l stainless steel. *Int J Fatigue* 70:163–170. <https://doi.org/10.1016/j.ijfatigue.2014.09.010>
- Sleeswyk A (1962) Emissary dislocations: theory and experiments on the propagation of deformation twins in α -iron. *Acta Metall* 10(8):705–725. [https://doi.org/10.1016/0001-6160\(62\)90040-8](https://doi.org/10.1016/0001-6160(62)90040-8)
- Smith M (2009) ABAQUS/Standard User's Manual, Version 6.9. Dassault Systèmes Simulia Corp, United States
- Sutcliffe J, Petherbridge J, Cartwright T, Springell R, Scott T, Darnbrough J (2019) Preparation and analysis of strain-free uranium surfaces for electron and x-ray diffraction analysis. *Mater Charact* 158:109968. <https://doi.org/10.1016/j.matchar.2019.109968>

- Tanaka K, Mura T (1981) A dislocation model for fatigue crack initiation. *J Appl Mech* 48(1):97–103. <https://doi.org/10.1115/1.3157599>
- Taplin D (1964) The mechanical properties and fracture of uranium. University of Oxford, Oxford
- Taplin D, Cocks G (1967) A note on creep-rupture mechanisms in reactor grade uranium. *J Nucl Mater* 23(2):245–248. [https://doi.org/10.1016/0022-3115\(67\)90073-6](https://doi.org/10.1016/0022-3115(67)90073-6)
- Taplin D, Martin J (1965) An effect of thermal cycling upon the ductility transition in alpha-uranium. *J Inst Met* 93:230–232
- Tarleton E (2020) CrystalPlasticity. GitHub Repository. <https://github.com/TarletonGroup/CrystalPlasticity>
- Tvergaard V (1981) Influence of voids on shear band instabilities under plane strain conditions. *Int J Fract* 17:389–407. <https://doi.org/10.1007/BF00036191>
- Williams D, Reid G (1971) A dynamic study of twin-induced brittle fracture. *Acta Metall* 19(9):931–937. [https://doi.org/10.1016/0001-6160\(71\)90086-1](https://doi.org/10.1016/0001-6160(71)90086-1)
- Woelke P, Shields M, Hutchinson J (2015) Cohesive zone modeling and calibration for mode I tearing of large ductile plates. *Eng Fract Mech* 147:293–305. <https://doi.org/10.1016/j.engfracmech.2015.03.015>
- Yamakov V, Saether E, Phillips D, Glaessgen E (2006) Molecular-dynamics simulation-based cohesive zone representation of intergranular fracture processes in aluminum. *J Mech Phys Solids* 54(9):1899–1928. <https://doi.org/10.1016/j.jmps.2006.03.004>
- Zamiri AR, Pourboghra F (2010) A novel yield function for single crystals based on combined constraints optimization. *Int J Plast* 26(5):731–746. <https://doi.org/10.1016/j.ijplas.2009.10.004>
- Zhou P, Xiao D, Wang W, Sang G, Zhao Y, Zou D, He L (2016) Twinning behavior of polycrystalline alpha-uranium under quasi static compression. *J Nucl Mater* 478:83–90. <https://doi.org/10.1016/j.jnucmat.2016.05.041>

Publisher's Note Springer Nature remains neutral with regard to jurisdictional claims in published maps and institutional affiliations.